

MECHANICAL BEHAVIOR OF METAL-COMPOSITE JOINTS
UNDER IMPACT RATES OF LOADING

By

David S. Gonzalez

A THESIS

Submitted to
Michigan State University
in partial fulfillment of the requirements
for the degree of

Mechanical Engineering - Master of Science

2014

ABSTRACT

MECHANICAL BEHAVIOR OF METAL-COMPOSITE JOINTS UNDER IMPACT RATES OF LOADING

By

David S. Gonzalez

Metal-Composite structures have a wide array of applications, most notably in the automotive, marine, and aerospace disciplines. The joining mechanism between the material constituents is arguably the most critical component of any structure. While the mechanical behavior of structural joints under static and cyclic loading conditions has been thoroughly investigated, very little research has been performed at impact rates of loading. Since virtually every structure is subjected to time-dependent stimuli, it is essential to understand the behavior of structural joints in the dynamic regime. In this study, a Split Hopkinson Pressure Bar (SHPB) was developed to induce an axial tensile stress pulse on Aluminum/S2-glass single-lap joints. The effect of joining method on strength and failure mode was investigated for bolted, bonded, and hybrid (bolted/bonded) joints at varying edge distance (e) to bolt diameter (d) ratios, a critical parameter in single-lap joints. It was demonstrated that joint strength increases with e/d and that failure mode transitions from catastrophic failure to progressive bearing damage between e/d 3 and 4. The findings also suggest that hybrid joints with lower e/d ratios exhibit comparable strength to bolted joints at higher e/d ratios. Effects of alternative material combinations and surface preparation on joint performance were also considered in Aluminum/E-glass and Advanced High Strength Steel (AHSS)/S2-glass single-lap bolted and hybrid joints. Additionally, the mechanical behavior of single-lap joints at elevated temperatures was investigated at 80°C. Both bolted and hybrid joints over the investigated range of e/d ratios exhibited a 20-30% decrease in joint strength. Design guidelines were established for single-lap structural joints with consideration for e/d ratio, joining method, material constituents, surface preparation, and environmental effects.

*I dedicate this work to my Lord and Savior Jesus Christ
and to my wife Theresa, my companion and best friend*

ACKNOWLEDGMENTS

I acknowledge the wise guidance of my research advisor, Dr. Tekalur. Thank you for enduring patiently while I “figured it out,” even though I gave you some reason to worry. I also acknowledge the incredible help, support, and companionship of my labmates and friends: Aishu, Wu Zhou, Andy, Abhishek, and Wei. To the undergraduate assistants Pete and Steve, who cut out more than a few cardboard pulse shapers for me; besides your willingness to do even the most mundane task, your willingness to learn was an inspiration. To the CVRC professors who have contributed so much to my learning and research experience: Dr. Gianaris, Dr. Cloud, Dr. Liu, Dr. Loos, Dr. Xiao, Dr. Haq, Dr. Li, Dr. Koricho, and Dr. Khomenko; thank you all for always being available to help. To Mike McLean and Adam Klein who taught me everything I now know about machining and without whom building my experiment would not have been possible. To my good friends who made my time at MSU a cherished experience I will carry with me for life: Karsten, Tim, Nariman, Todd, Steve, Nick Kamar, Nick Kuuttila, Dan, Miao, Shi, Vahid, Martin, Abdul, Chris C., and Ali. I’d like to especially acknowledge Dr. Katy Colbry. Thank you so much for your friendship and for helping me and my family make it through these two years. We honestly could not have done it without you. Last, but not least, I acknowledge TARDEC for sponsoring the research and finding the work to be an investment to the engineering community.

TABLE OF CONTENTS

LIST OF TABLES	vi
LIST OF FIGURES	vii
KEY TO SYMBOLS.....	xi
CHAPTER 1: Introduction to Joining and Impact Test Methods	1
1.1 Joining Methods.....	1
1.2 Key Parameters	3
1.3 Impact Test Methods: Discussion.....	7
1.4 Impact Test Methods: Split-Hopkinson Pressure Bar History.....	8
1.5 Impact Test Methods: Split-Hopkinson Pressure Bar Theory	10
CHAPTER 2: Design of a Split-Hopkinson Tension Bar (SHTB) for Testing Structures... 18	
2.1 Design Considerations for Structural Testing.....	18
2.2 SHTB Construction.....	20
2.3 System Validation.....	27
CHAPTER 3: Mechanical Behavior of Bolted, Bonded, and Hybrid (Bolted/Bonded) Metal-Composite Joints under Impact Loading Conditions	32
3.1 Materials and Methods.....	32
3.2 Joint Behavior under Static Loading.....	34
3.3 Joint Behavior under Impact Loading.....	43
3.4 Effect of Different Materials on Mechanical Behavior	54
3.5 Effect of Surface Preparation on Mechanical Behavior	59
3.6 Effect of Elevated Temperature on Mechanical Behavior.....	61
CHAPTER 4: Conclusion	63
4.1 Concluding Remarks.....	63
4.2 Future Scope of Work.....	64
REFERENCES.....	65

LIST OF TABLES

Table 1: Types of impact and equivalent strain rates.	8
--	---

LIST OF FIGURES

Figure 1: Basic types of adhesive joints. [1].....	2
Figure 2: Variation of bearing strength of $0^\circ/\pm 45^\circ$ laminates with w/d ratio. $d = 6.35$ mm, $t = 3$ mm, $\sigma_z = 12$ MPa. [4].....	4
Figure 3: Effect of d/t ratio on bearing strength of $0^\circ/\pm 45^\circ$ laminates of G/69. d/t values as indicated. [4].....	5
Figure 4: Variation of bearing strength of $0^\circ/\pm 45^\circ$ laminates with e/d ratio. $d = 6.35$ mm, $t = 3$ mm, $\sigma_z = 12$ MPa. [4].....	6
Figure 5: Standard test methods for desired strain rates ranging from 0 to 10^8 s ⁻¹	7
Figure 6: Apparatus developed by B. Hopkinson for the measurement of pressure produced by the detonation of gun cotton. [20, 21].....	9
Figure 7: Schematic of Kolsky's apparatus. [21, 23].....	10
Figure 8: Simplified schematic of a Split-Hopkinson Pressure Bar a) in compression; and b) in tension.	11
Figure 9: Lagrange spatial-time diagram of wave propagation within a compression SHPB.....	13
Figure 10: Incident bar-specimen and transmission bar-specimen interfaces as functions of stress pulse displacements.	15
Figure 11: Tensile SHPB at Composite Vehicle Research Center, MSU.....	20
Figure 12: Compressed nitrogen gas delivery system.	20
Figure 13: Impact region of SHTB showing striker, anvil, and momentum trap on Teflon PTFE track.....	21
Figure 14: Schematic of specimen grip fixtures.	22
Figure 15: SHTB grip fixture assembly and temperature chamber.	23
Figure 16: Exploded view model of temperature chamber for SHTB.....	24
Figure 17: Diametrically opposed resistance strain gauges in 3 lead-wire $\frac{1}{4}$ bridge Wheatstone circuit configurations in incident bar.	24
Figure 18: SHTB data acquisition system including 4-channel Lecroy WaveJet 354A digital oscilloscope, Vishay 2310B signal conditioning amplifiers (4), and 10-channel Omega MDSSi8 benchtop indicator (left to right).	25
Figure 19: SHTB high speed imaging system including Vision Research Phantom V12.0 high-speed camera and Phantom camera control software	26

Figure 20: SHTB laser triggering system including Eaton comet series photoelectric sensor (left) along with Altech 24VDC power supply and Phoenix Contact optocoupler (right)	26
Figure 21: Scaled model of SHTB set-up and corresponding Lagrange diagram.	28
Figure 22: Temperature chamber with 4 thermocouples (left) and diagram with thermocouple locations (right).....	30
Figure 23: Temperature chamber validation experiments (3) - Temperature vs. time graphs at 4 thermocouple locations.	30
Figure 24: Thermal imaging camera results of temperature vs. image distance for area surrounding temperature chamber (left) and in bar (right) over 12 minutes.	31
Figure 25: MTS 810 Material Testing System used for static testing at 1 mm/min crosshead displacement.	33
Figure 26: Models and schematics with dimensions of single-lap a) static specimens and b) SHTB specimens.....	34
Figure 27: Aluminum/S2-glass single-lap joints tested statically in a MTS 810 system.	35
Figure 28: Load-displacement curve for bolted single-lap joint, $e/d = 1$	36
Figure 29: Load-displacement curves for bolted single-lap joints, $e/d = 1-4$	36
Figure 30: Common failure modes for bolted assemblies and representative equations. [9]	37
Figure 31: Observed failure modes for Aluminum/S2-glass bolted joints, $e/d = 1-4$, under static loading.....	38
Figure 32: Load-displacement curves for bonded and bolted single-lap joints, $e/d = 1$ and 4.	39
Figure 33: Common failure modes for bonded single-lap joints. [31]	40
Figure 34: Observed failure modes for Aluminum/S2-glass bonded joints under static loading. 40	
Figure 35: Load-displacement curves for bonded and bolted single-lap joints, $e/d = 1$ (top), and hybrid single-lap joint, $e/d = 1$ (bottom).....	41
Figure 36: Load-displacement curves for hybrid single-lap joints, $e/d = 1-4$ (left) and bolted single-lap joints, $e/d = 1-4$ (right).	42
Figure 37: Observed failure modes for Aluminum/S2-glass bolted and hybrid joints, $e/d = 1-4$, under static loading	43
Figure 38: Aluminum/S2-glass single-lap joints tested dynamically in a SHTB.	44
Figure 39: Load vs. time curves for bolted joint $e/d=1$ for static (top) and impact (bottom) loading conditions.....	45

Figure 40: Load-time behavior of a bolted joint, $e/d = 1$, subjected to impact with high speed images at 4 points along the loading event.	46
Figure 41: High speed images of joint slip and bolt rotation in bolted joint, $e/d = 1$, subjected to impact.	47
Figure 42: Observed failure modes for Aluminum/S2-glass bolted joints, $e/d = 1-4$, under static and impact loading.	48
Figure 43: Load-time behavior of a bolted joint, $e/d = 1$, subjected to impact with high speed images at 4 points along the loading event.	49
Figure 44: Interlaminar crack initiation in bonded joint from 104-112 μ s.	49
Figure 45: Load-time behavior of a hybrid joint, $e/d = 1$, subjected to impact with high speed images at 5 points along the loading event.	50
Figure 46 Observed failure modes for Aluminum/S2-glass hybrid joints, $e/d = 1-4$, under static and impact loading.	51
Figure 47: Peak loads of bolted, bonded, and hybrid joints, $e/d = 1-4$, under static loading.	52
Figure 48: Failure loads of bolted, bonded, and hybrid joints, $e/d = 1-4$, under static loading.	52
Figure 49: Failure loads of bolted and hybrid joints, $e/d = 1-4$, at static, low velocity (intermediate), and impact loading conditions.	53
Figure 50: Failure loads of Aluminum/S2-glass and Aluminum/E-glass bolted and hybrid joints, $e/d = 1$ and 4, under impact loading.	54
Figure 51: Observed failure modes for Aluminum/S2-glass and Aluminum/E-glass bolted and hybrid joints, $e/d = 1$ and 4, under impact loading.	55
Figure 52: Failure loads of Aluminum/S2-glass and Advanced High Strength Steel/S2-glass bolted joints, $e/d = 1-4$, under impact loading.	56
Figure 53: Observed failure modes for Aluminum/S2-glass and Advanced High Strength Steel/S2-glass bolted joints, $e/d = 1-4$, under impact loading.	57
Figure 54: Failure loads of Advanced High Strength Steel/S2-glass bolted joints, $e/d = 1-4$, and hybrid joints, $e/d = 1$ and 2, under impact loading.	58
Figure 55: Observed failure modes for Advanced High Strength Steel/S2-glass hybrid joints, $e/d = 1$ and 2, under impact loading.	58
Figure 56: Failure loads of Aluminum/S2-glass bolted and hybrid joints, $e/d = 1-4$, and anodized hybrid joints, $e/d = 1$ and 2, under impact loading.	59
Figure 57: Failure loads of Advanced High Strength Steel/S2-glass bolted joints, $e/d = 1-4$, and hybrid joints with and without commercial surface preparation, $e/d = 1$ and 2, under impact loading.	60

Figure 58: Failure loads of Aluminum/S2-glass bolted and hybrid joints, $e/d = 1$ and 4, at room temperature and 80°C under impact loading 61

KEY TO SYMBOLS

A_b	bearing area
A_{bar}	cross-sectional area of bar
A_s	cross-sectional area of specimen
c_{bar}	stress wave propagation speed in incident and transmission bars
c_{str}	stress wave propagation speed in striker
C	voltage/strain conversion factor
d	bolt diameter
$\partial/\partial\tau$	partial time derivative
$\partial/\partial x$	partial spatial derivative
e	edge distance
E	Young's Modulus
E_{bar}	Young's Modulus of incident and transmission bars
ε	strain
$\varepsilon_1, \varepsilon_2$	interfacial strain
ε_{bar}	strain in bar
$\varepsilon_I, \varepsilon_R, \varepsilon_T$	resultant bar strain from incident, reflected, and transmitted stress pulses
$\dot{\varepsilon}_s$	average strain rate in specimen
f, g	functions
F_a	applied force
F_{bar}	force in incident and transmission bars
l_s	length of specimen
l_{str}	length of striker

ρ_{bar}	density of incident and transmission bars
R_{bar}	radius of bar
σ	stress
σ_1, σ_2	interfacial stress
σ_b	bearing strength/bearing stress
$\sigma_{b(ult)}$	ultimate bearing strength
σ_s	uniform stress in specimen
σ_z	clamping pressure
t	thickness
t_{wave}	time duration of stress pulse
τ	time
u	displacement
\dot{u}	particle velocity
u_1, u_2	interfacial displacements
u_I, u_R, u_T	resultant bar displacements from incident, reflected, and transmitted stress pulses
V_{sg}	strain gauge voltage output
x	distance
w	width

CHAPTER 1: Introduction to Joining and Impact Test Methods

1.1 Joining Methods

In any mechanical system, great care must be taken when designing the mechanism that joins two or more materials or components together. This interface between materials is often the most critical with respect to structural integrity since it provides the continuity of load transference through a structure. Two of the most commonly employed joining methods are fastening and adhesively bonding, both containing great diversity of available options and applications.

Fasteners such as pins, screws, and bolts are often used because they allow for the non-destructive disassembly and easy reassembly of structures which is essential for timely and cost effective maintenance and repair. Fasteners also have the added benefit of being insensitive to environmental factors such as heat and humidity so long as corrosion preventative measures are taken. One of the major disadvantages of fasteners is that they inherently require holes to be introduced to the joining materials. In the case of composite-fiber materials, this requires partial removal of reinforcing fibers which give these types of composites their strength. Regardless of the material used, high stress concentrations are found in the locations surrounding the hole. In the case of bolted joints which typically require specified torque requirements, periodic maintenance is also required due to the relaxation of the bolt preload caused by vibrations.

Adhesive joints come in a variety of configurations, such as those shown in **Figure 1** [1], and are superior to fasteners in several different arenas. First of all, they offer considerable weight reduction than their fastener counterparts which, from an automotive, marine, or aerospace perspective, directly translates to fuel economy and mechanical efficiency. Fatigue resistance is another added benefit to adhesive joints, as well as uniform stress distribution under

load which is desirable for load bearing capability. Materials bonded using structural adhesives typically display increased peak strength than fasteners as well. However, adhesive joints are not commonly used where efficient disassembly and reassembly is required. They are highly sensitive to surface preparation and environmental conditions, especially moisture and corrosive conditions. They are difficult to inspect without more sophisticated and consequently more costly inspection methods making defects and damage difficult to detect. Lastly, failure in bonded joints is catastrophic in nature, offering no load bearing capacity post-failure which makes using adhesive joints potentially more risky.

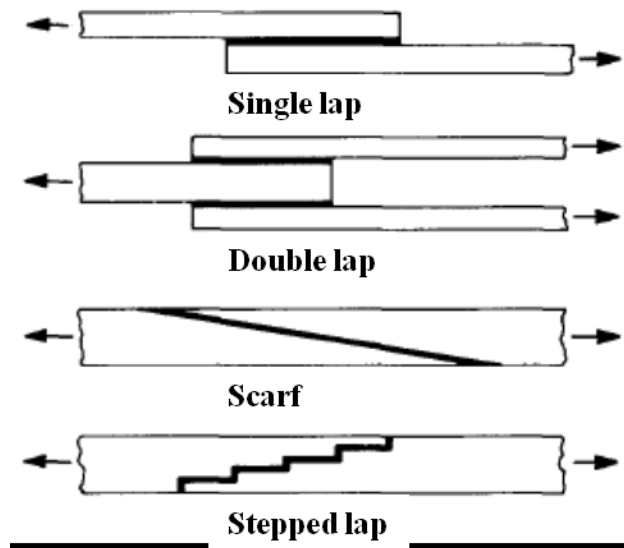


Figure 1: Basic types of adhesive joints. [1]

The use of a hybrid combination of both fastening and bonding has gained more attention in industry over recent decades. While hybrid joints do combine some of the best properties of fastened and bonded joints, their performance is difficult to experimentally measure and scientifically predict. Joint strength, for example, in a hybrid joint is not the summation of the strengths of a purely bonded and a purely fastened joint because the individual stiffnesses in each load path differ [2,3]. Due to the complex interaction between the constituents of a hybrid joint and the numerous variables that affect those interactions, modeling their behavior with any

degree of predictive accuracy is difficult. A better understanding of the physics behind hybrid joints is needed, especially those subjected to time dependent loading conditions.

This investigation was carried out as an initiative to understand the mechanical behavior of dissimilar material joints subjected to impact loading conditions for the Army's Tank Automotive Research, Development and Engineering Center (TARDEC). The particular focus was on joining fiberglass panels to different types of metallic panels using a combination of fasteners and structural adhesives. The single lap joint configuration shown in **Error! Reference source not found.** was chosen in this study due to its practicality in automotive design and simplicity for understanding new phenomena.

1.2 Key Parameters

There are various material and geometric parameters to consider in the design of any structural joint. For the single lap hybrid (bolted/bonded) joints in this investigation, these parameters include the selection of materials, ply orientation (in composites), bolt/washer/nut configurations, bolt preload, bolt hole clearance, adhesive type, bond area, surface preparation and the geometric ratios between the width (w), thickness (t), bolt diameter (d) and the distance from the bolt center to the edge (e). The latter set of parameters have been exhaustively studied for single lap joints subjected to static and cyclic loading conditions and have been presented here for a clear understanding of the parameters chosen in this study.

Kretsis and Matthews [4] studied the effect of different joint geometries, clamping pressure, σ_z , and ply orientations on the strength and failure modes of E-glass fiber (G) and XAS carbon fiber (XAS) composite double lap joints with two different types of resins, Fothergill Code 69 and Ciba-Geigy 913 (designated G/69, G/913, XAS/69, and XAS/913 in the following

figures). **Figure 2** shows the variation of ultimate bearing strength of $0^\circ/\pm 45^\circ$ laminates with w/d ratio for each of the aforementioned material combinations. Ultimate bearing strength, $\sigma_{b(ult)}$, is determined by the ultimate bearing load divided by the area that is the product of the bolt diameter and specimen thickness. The composite materials were bolted to steel test coupons in a double lap configuration, fitted with a bolt torque load cell, and loaded axially in tension in a 100 kN Instron test machine. Bolt diameter, laminate thickness, and preload were kept constant at 6.35 mm, 3 mm, and 12 MPa respectively. As shown in the graph, bearing strength increases as w/d increases until it plateaus at approximately $w/d = 3.2$. It's in this asymptotic region that failure mode changes from tension to bearing mode. In the tension mode of failure, the composite fails across the width of the material with cracks originating at the hole locations perpendicular to the loading direction. Bearing failure is a progressive mode of failure which

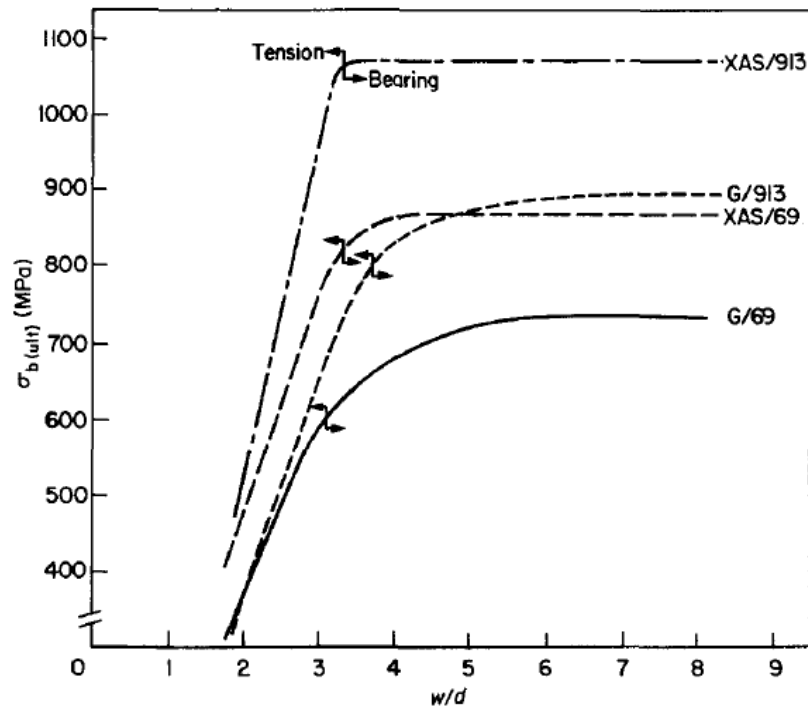


Figure 2: Variation of bearing strength of $0^\circ/\pm 45^\circ$ laminates with w/d ratio. $d = 6.35$ mm, $t = 3$ mm, $\sigma_z = 12$ MPa. [4]

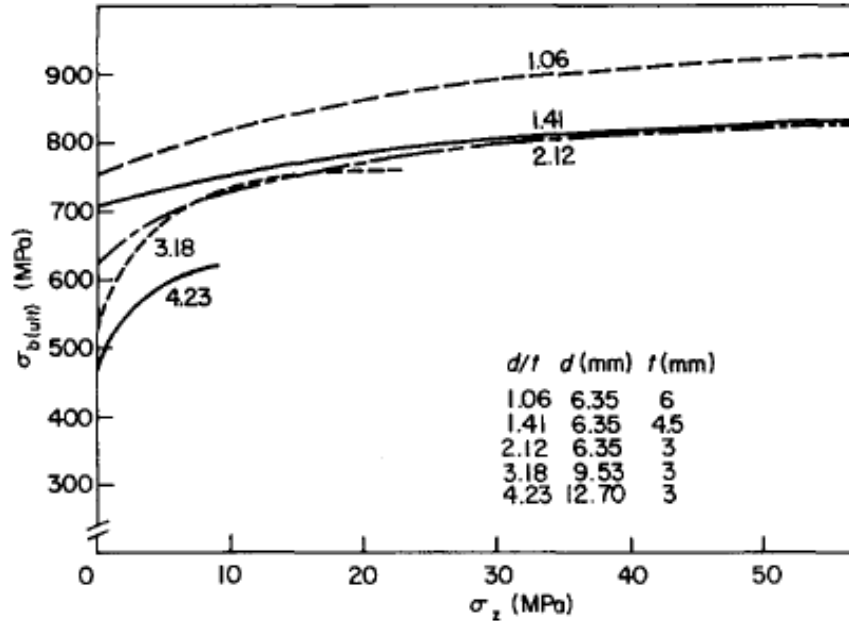


Figure 3: Effect of d/t ratio on bearing strength of $0^\circ/\pm 45^\circ$ laminates of G/69. d/t values as indicated. [4]

constitutes the accumulation of damage from fiber micro-buckling, fiber–matrix shearing, and matrix compression failure [5].

Another geometric parameter that Kretsis and Matthews investigated was the effect of d/t ratio on the bearing strength of $0^\circ/\pm 45^\circ$ G/69 laminates across a wide range of preloads, illustrated in **Figure 3**. Several key observations were made, including a reduction in ultimate bearing strength in thinner materials. Another limitation to thinner materials is that they do not support higher preloads where the lateral pressure from torque becomes high enough to deform the laminate. It was also observed that out of plane buckling occurs in laminates where $d/t > 3$. As a result, Kretsis and Matthews recommended a range of $1 < d/t < 3$ due to the buckling in thicker materials and the strength and preload limitations of thinner materials.

Lastly, the variation of bearing strength of $0^\circ/\pm 45^\circ$ laminates with e/d ratio is shown in **Figure 4**. In similar fashion to the effect of w/d , ultimate bearing strength also increases asymptotically as e/d increases with a change in failure mode within this asymptotic region.

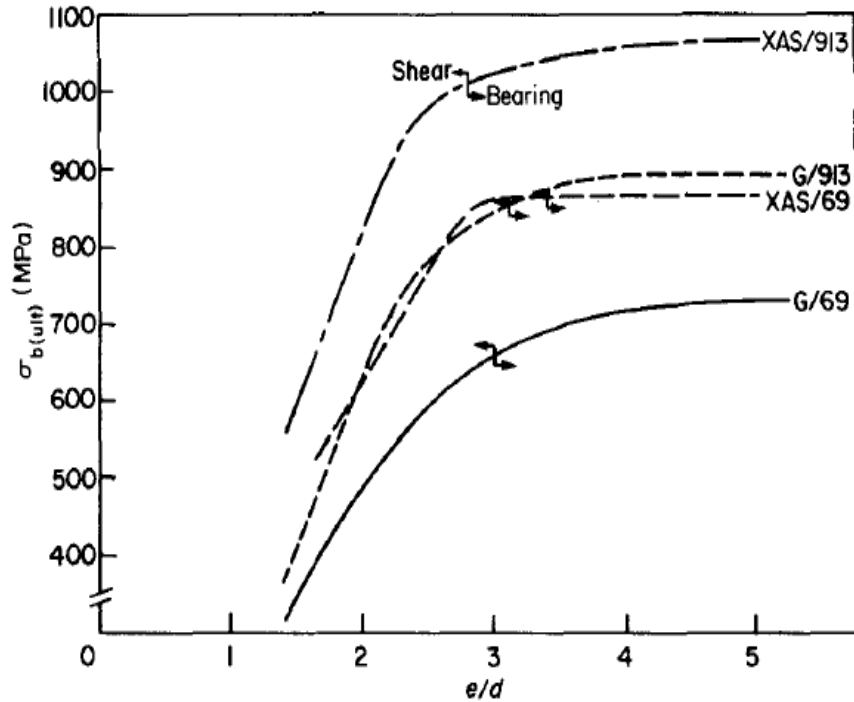


Figure 4: Variation of bearing strength of $0^\circ/\pm 45^\circ$ laminates with e/d ratio. $d = 6.35$ mm, $t = 3$ mm, $\sigma_z = 12$ MPa. [4]

Instead of a tension-bearing mode transition in the case of w/d , here the transition is from shear to bearing failure. Shear failure, like tension failure, is catastrophic in nature and also initiates as cracks at the bolt hole locations, this time though in the direction of the applied load.

Although the Kretsis and Matthews analysis is presented here, a significant number of studies confirm the abovementioned results for w/d , d/t , and e/d [5–16]. Due to the unanimity of these results, the key parameters were selected for the current investigation with a high degree of confidence. Based on the prescribed tank and automotive application of a metal-composite single-lap joint, e/d was chosen as the variable parameter because it has direct influence on the amount of material used, and consequently cost, while w/d would only influence bolt spacing in a multi-bolt joint (not the subject of this investigation). The constants $w/d = 4$ and $d/t = 2$ were then chosen to maximize the strength of the e/d variable. Although many more parameters affect joint performance as previously stated, these proven significant geometric parameters were

chosen in order to understand the basic physics driving mechanical behavior of dissimilar material joints subjected to impact loading conditions.

1.3 Impact Test Methods: Discussion

Over the past several decades, design guidelines have been developed for numerous material and geometric properties based on the results from experimental, numerical, and analytical investigations of single-lap joints subjected to static loads. However, effective characterization of mechanical behavior necessitates evaluation at realistic loading conditions. Virtually every structure experiences some form of time-dependent loading condition and often, as in automotive, marine, and aerospace applications, impact loading is especially critical for design considerations.

The time rate of change of strain, or “strain-rate,” is often used to describe the rate at which deformation occurs within a material [17]. **Figure 5** illustrates testing methods applicable to the desired strain rate effects for material characterization. Strain rates spanning 10^{-6} to 10^{-1} s^{-1}

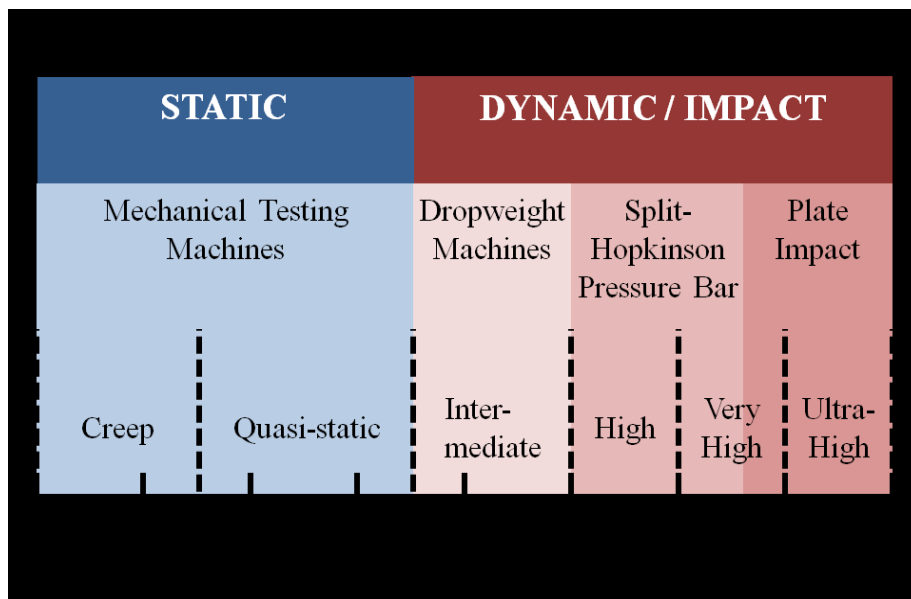


Figure 5: Standard test methods for desired strain rates ranging from 0 to 10^8 s^{-1} .

Table 1: Types of impact and equivalent strain rates.

Impact Type	Velocity (km/s)	Example	Equivalent Strain Rate
Crash	0.2 - 0.4	Vehicle Crash	High
Ballistic	1 - 2	Bullet	Very high
Hypervelocity	>5	Asteroid Impact	Ultra-high

are often associated with the aforementioned static testing methods, while rates ranging from 10^{-1} to 10^2 , 10^2 to 10^4 , 10^4 to 10^6 , and 10^6 to 10^8 s^{-1} correspond to intermediate, high, very high, and ultra-high strain rates respectively [18]. Different types of impact conditions and their equivalent strain rates are shown in **Table 1**. For most structures, especially those in tank and automotive applications, it is appropriate to consider crash and ballistic type impacts, those pertaining to high and very high strain rates.

Material characterization under impact loading conditions has been conducted for a number of different materials and it is generally understood that most materials exhibit strain rate sensitive behavior. As loading rate increases, flow stress in the material increases along with a decrease in material toughness [19]. Unfortunately, this form of experimental investigation has not been extrapolated beyond materials to structures. The objective of the current investigation is to characterize the net effect of the rate sensitive material constituents within bolted, bonded, and hybrid (bolted/bonded) single-lap joints subjected to impact. Since high and very high strain rates corresponding to crash and ballistic type impacts are desired, the Split-Hopkinson Pressure Bar was chosen as the viable test method for this study.

1.4 Impact Test Methods: Split-Hopkinson Pressure Bar History

In 1914, British engineer Bertram Hopkinson developed the first Hopkinson bar shown in **Figure 6** [20,21]. The experiment consisted of a long bar suspended from two sets of wires

aligned with a suspended box. A short rod was held in place at end of the long rod by a small magnetic force. A bullet was then shot at the end of the long bar causing a pressure wave to propagate down the bar and the short rod to fly off into the box. The displacement of the box was then measured from which the momentum and maximum pressure of the wave in the long rod was determined. One obvious limitation to Hopkinson's approach was that it could only measure the final displacement and not the history over the entire loading event.

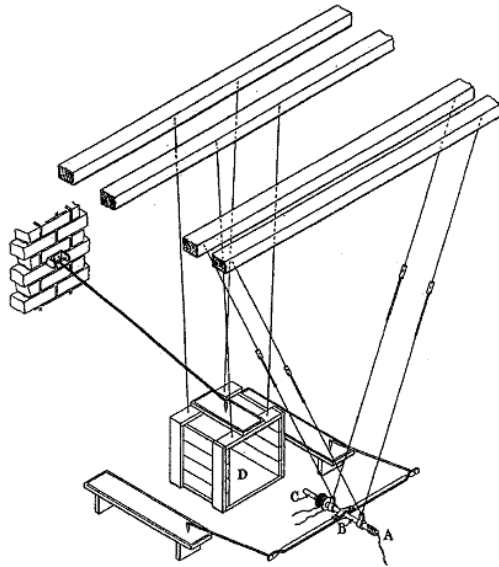


Figure 6: Apparatus developed by B. Hopkinson for the measurement of pressure produced by the detonation of gun cotton. [20, 21]

In 1948, Welsh physicist Rhisiart Davies was able to obtain the pressure-time curve for the entire pulse by taking electronic measurements at the free end of the Hopkinson bar using cathode ray oscilloscopes and electrical condenser units [21,22]. A year later, Herbert Kolsky lengthened the short rod in Hopkinson's experiment and used the two bars in series to create what is today known as the split-Hopkinson pressure bar (SHPB), also known as the Kolsky bar. Kolsky's experimental set-up is depicted in **Figure 7** [21,23].

In 1960, Harding was able to convert the SPHB into a tension test by allowing the initial compressive wave to pass by the specimen into the second bar by means of a collar. The wave

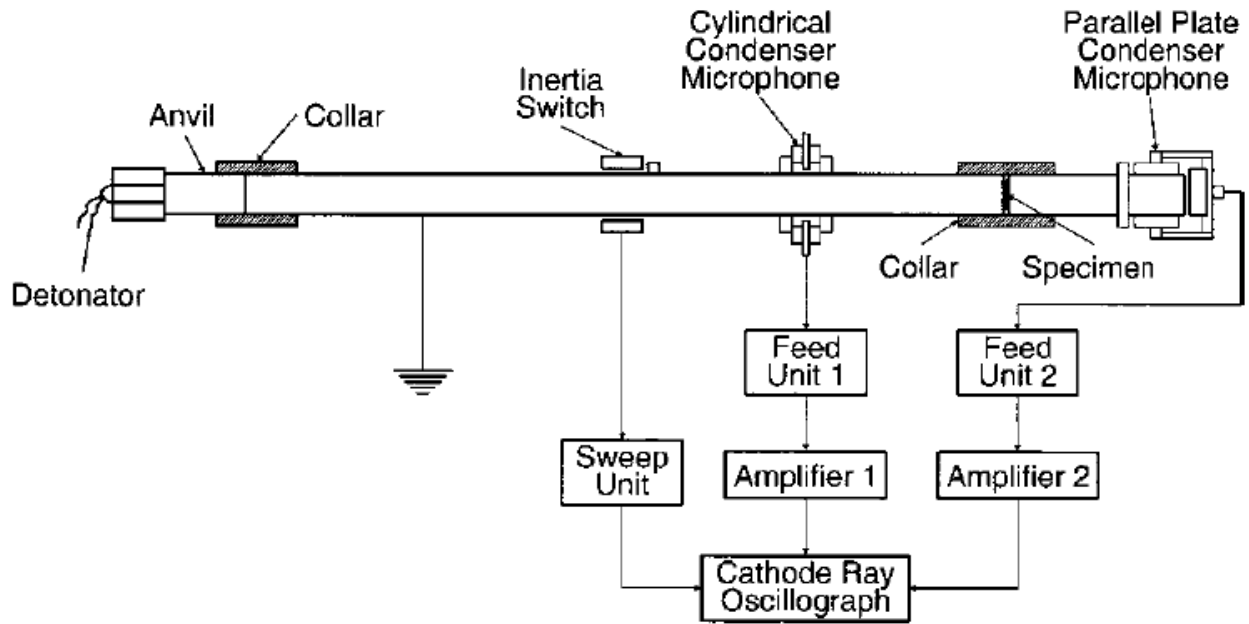


Figure 7: Schematic of Kolsky's apparatus. [21, 23]

was then reflected at the free end as a tension wave which was then passed into the specimen [24]. In 1984, Kinya Ogawa modified Harding's design to create the modern day tension SHPB which uses a projectile propelled by a gas gun to impact a flange at end of incident bar [25]. There have been numerous advancements since this time including the development of torsion SPHBs and the use of optical devices in conjunction with pressure wave data.

1.5 Impact Test Methods: Split-Hopkinson Pressure Bar Theory

When an impact occurs in a structure, three types of phenomena occur: 1) stress or shock waves are propagated in the structure, 2) large deformations develop leading to failure, and 3) excitation occurs in the impacted structure [18]. There are four categories of impact tests that correspond to the properties desired for investigation. These impact tests include high strain rate experiments, wave-propagation experiments, dynamic failure experiments, and direct impact experiments. In SHPB experiments, the high-strain rate properties of a material are desired.

The most common SHPB set-up is the compression bar illustrated in **Figure 8a**. The set-up consists of two long bars, the incident bar and the transmission bar, which are used in series as force transducers to transfer the time dependent load from the impact to the specimen. These bars deform elastically throughout the test and are usually made of high strength steel, although other materials can be used depending on the specimen material. A compressed gas is used to charge a barrel which accelerates the projectile, called the striker, down it. The striker impacts the end of the incident bar causing a compressive stress pulse to propagate through the bar. When the stress pulse reaches the specimen, it partially transmits into the specimen and partially reflects back into the incident bar as a tension wave as a result of the impedance mismatch between the bar and the specimen. Strain gages are placed on both the incident and transmission

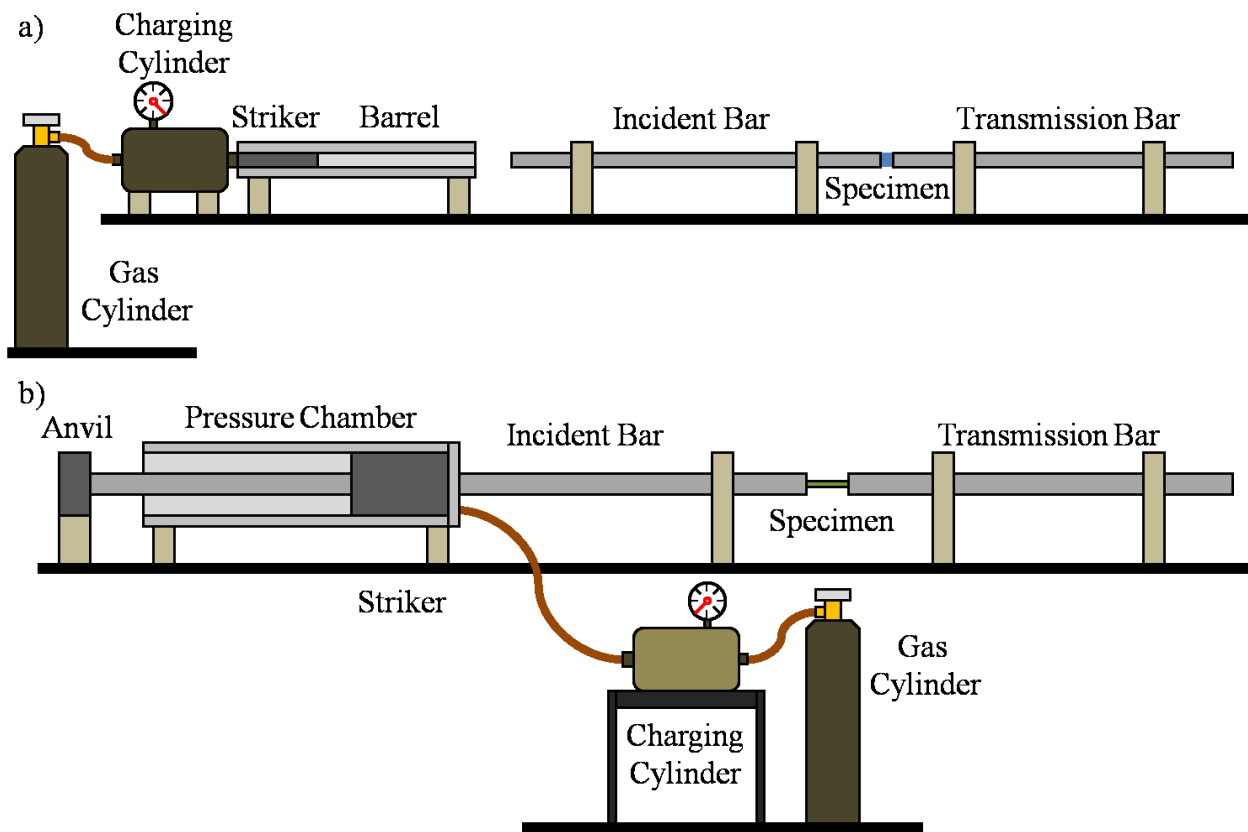


Figure 8: Simplified schematic of a Split-Hopkinson Pressure Bar
 a) in compression; and b) in tension.

bars in a Wheatstone bridge circuit configuration. The voltage output from the gages is transmitted to a signal amplifier and then a digital oscilloscope for capturing the strain history.

Another common SHPB experimental set-up is the tension bar shown in **Figure 8b**. Similar to the compression bar, the tension bar also uses incident and transmission bars as force transducers. Compressed gas is again used to accelerate the striker down the barrel. In this case however the striker rides on the incident bar and impacts a flange called the anvil which is rigidly connected to the end of the incident bar. A tension stress pulse propagates down the bar and into the specimen. The portion of the stress pulse reflected back at the end of the incident bar is compressive in nature while the tensile pulse transmits further into the transmission bar. An understanding of wave mechanics is necessary in order to determine the specimen response from the strain histories of both incident and transmission bars. Although a tensile SHPB was used in the present study, an overview of the wave mechanics within a compressive SHPB is presented here for a more simplistic explanation.

Unlike static tests, experimental conditions in a Hopkinson bar are determined through trial tests based on the specimen response. **Figure 9** gives a visual representation of one wave cycle in a compression SHPB experiment. When the striker impacts the incident bar, a compressive stress pulse twice the length of the striker is produced. The resistance strain gages (RSGs) are placed at the middle of the incident and transmission bars to prevent wave interference of the transmitted and reflected stress pulses. The specimen is generally a different material than the bars and smaller in cross-sectional area, creating a difference in the mechanical impedance between the incident bar and the specimen which again allows for a portion of the wave to be reflected back into the bar. The length of the specimen is also comparatively small to the length of the stress pulse, allowing for stress equilibrium to be attained because of several

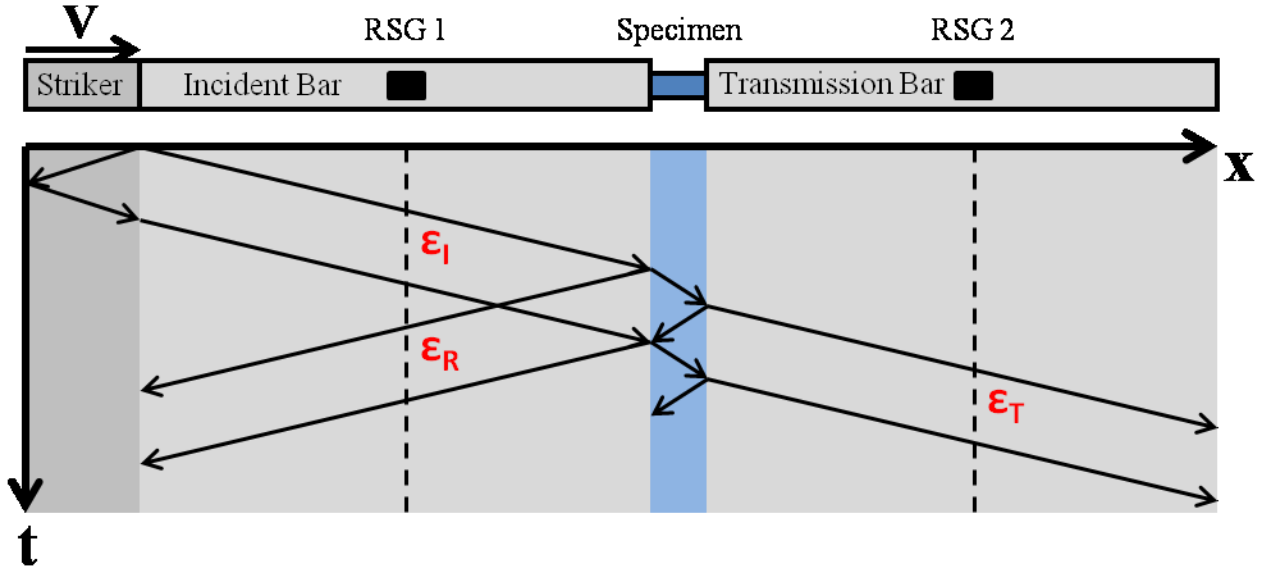


Figure 9: Lagrange spatial-time diagram of wave propagation within a compression SHPB.

reflections of the wave within the specimen prior to failure. Attaining stress equilibrium is vital, as it allows for the relation of measured strain in the bar to the strain experienced by the specimen.

The analysis begins with the governing differential equation of one-dimensional longitudinal motion for an elastic bar given by

$$\frac{\partial}{\partial x} \left(EA \frac{\partial u}{\partial x} \right) = \rho A \frac{\partial^2 u}{\partial \tau^2} \quad (1.1)$$

where E is the modulus of elasticity, A is the cross-sectional area, ρ is the density, and u is the displacement. In the case of SHPB experiments, the incident and transmission bars have a constant cross-sectional area and modulus of elasticity, reducing the general equation to

$$\frac{\partial^2 u}{\partial x^2} = \frac{\rho}{E} \frac{\partial^2 u}{\partial \tau^2} \quad (1.2)$$

It is convenient in wave mechanics to rearrange the equation in terms of wavespeed, c . The governing equation further reduces to

$$\frac{\partial^2 u}{\partial x^2} = \frac{1}{c^2} \frac{\partial^2 u}{\partial \tau^2} \quad (1.3)$$

where

$$c = \sqrt{\frac{E}{\rho}} \quad (1.4)$$

The general solution to the governing equation is then found by the classical d'Alembert solution to the one-dimensional wave equation and is given as a combination of two arbitrary functions of distance, wavespeed, and time:

$$u = f(x - c\tau) + g(x + c\tau) \quad (1.5)$$

Using the general solution, the strain, ε , experienced by the bars can be expressed as the spatial derivative of the displacement

$$\varepsilon = \frac{\partial u}{\partial x} = \frac{\partial f}{\partial x} + \frac{\partial g}{\partial x} = \dot{f} + \dot{g} \quad (1.6)$$

From the stress-strain relationship for isotropic materials, the stress in the bars can then be calculated by

$$\sigma = E(\dot{f} + \dot{g}) \quad (1.7)$$

Finally, the particle velocity of the pulse in the bar, \dot{u} , is determined by the time derivative of the displacement as

$$\dot{u} = \frac{\partial u}{\partial \tau} = -c\dot{f} + c\dot{g} = c(-\dot{f} + \dot{g}) \quad (1.8)$$

In order to determine relevant information about the specimen, a relationship is needed to relate the stress state in the bars to the stress state in the specimen. To obtain this, the interfaces between the incident and transmission bars and the specimen are considered. **Figure 10** illustrates these interfaces. The displacement at interface 1, u_1 , can be equated to the

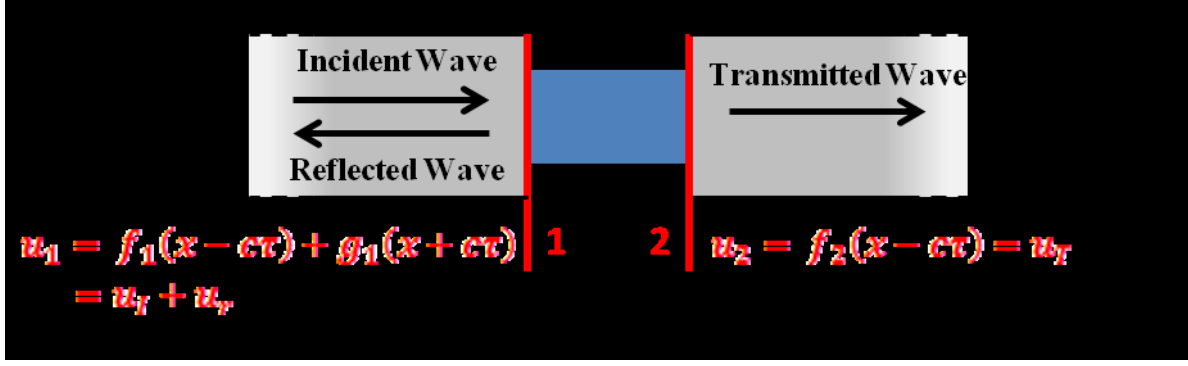


Figure 10: Incident bar-specimen and transmission bar-specimen interfaces as functions of stress pulse displacements.

displacement resulting from both the incident and reflected waves while the displacement at interface 2, u_2 , is only a function of the displacement resulting from the transmitted wave given by

$$u_1 = f_1(x - c\tau) + g_1(x + c\tau) = u_I + u_r \quad (1.9)$$

and

$$u_2 = f_2(x - c\tau) = u_T \quad (1.10)$$

From **Equations (1.6) - (1.10)**, the strain, stress, and particle velocity at each interface is given by

$$\varepsilon_1 = \frac{\partial u_1}{\partial x} = \dot{u}_I + \dot{u}_R = \varepsilon_I + \varepsilon_R \quad (1.11)$$

$$\varepsilon_2 = \frac{\partial u_2}{\partial x} = \dot{u}_T = \varepsilon_T \quad (1.12)$$

$$\sigma_1 = E_{bar}(\varepsilon_I + \varepsilon_R) \quad (1.13)$$

$$\sigma_2 = E_{bar}\varepsilon_T \quad (1.14)$$

$$\dot{u}_1 = c(-\varepsilon_I + \varepsilon_R) \quad (1.15)$$

$$\dot{u}_2 = -c\varepsilon_T \quad (1.16)$$

If uniform stress distribution is assumed, again, because the length of the specimen is much smaller than the length of the pulse, then the stress in the specimen is calculated as the average stress between the 2 interfaces as follows

$$\sigma_s = \frac{\sigma_1 A_{bar} + \sigma_2 A_{bar}}{2A_s} = \frac{E_{bar} A_{bar}}{2A_s} (\varepsilon_I + \varepsilon_R + \varepsilon_T) \quad (1.17)$$

where A_{bar} is the cross-sectional area of the bar and A_s is the cross-sectional area of the specimen.

The average strain rate experienced by the specimen can also be determined as the difference in particle velocity at the interfaces over the length of the specimen, l_s , as follows

$$\dot{\varepsilon}_s = \frac{\dot{u}_2 - \dot{u}_1}{l_s} = \frac{c}{l_s} (-\varepsilon_T + \varepsilon_I - \varepsilon_R) \quad (1.18)$$

Assuming uniform deformation,

$$\varepsilon_I + \varepsilon_R \cong \varepsilon_T \quad (1.19)$$

These equations can be simplified even further to

$$\sigma_s = \frac{E_{bar} A_{bar}}{A_s} \varepsilon_T \quad (1.20)$$

$$\dot{\varepsilon}_s = -\frac{2c}{l_s} \varepsilon_R \quad (1.21)$$

Equations (1.20) and (1.21) give the relationships for stress and strain in the specimen based on the strain experienced by the incident and transmission bars. As previously mentioned, these relationships assume a uniform stress distribution within the specimen, making them useful for characterizing dynamic material properties of materials. However, in the case of the single-lap joints in this investigation, uniformity of stress does not exist. In fact, elasticity theory shows that for a homogenous material, the stress is 3 times greater at the bolt hole locations perpendicular to the loading direction than a far field stress away from the hole. Since the strain, stress, and displacement vary within the joint, the classical Hopkinson bar theory cannot be

employed and only the load and load profile that is transmitted through the specimen into the transmission bar post failure can be observed. For this reason, the term “loading rate” replaces “strain rate” and the mechanical behavior vice mechanical properties are discussed.

CHAPTER 2: Design of a Split-Hopkinson Tension Bar (SHTB) for Testing Structures

2.1 Design Considerations for Structural Testing

One of the major challenges with the SHPB test method is that experimental conditions are determined through trial tests based on the specimen response. Experimental set-up therefore can be very time intensive as a successful experiment is attained by trial and error primarily by altering specimen sizes and geometries and using pulse shaping techniques. The effects of dispersion must be taken into account, since shorter stress pulses with sharper rise times cause greater dispersion because of high frequency and wider range. Pulse shaping materials in this case result in longer rise time, wider pulse width, and consequently lower dispersion.

Another factor to consider is the necessity of uniform deformation and stress equilibrium in the specimen in order to accurately predict the strain and stress state within it. This is achieved by keeping the length of the specimen much smaller than the incident pulse width. Some optical methods have been used in the past to ascertain the stress state of the specimen with varying degrees of success, but such methods are generally difficult to employ and not useful for all materials. When testing structures, uniform deformation and stress equilibrium are not achievable, so comparative tests with different gage lengths are necessary.

It is also important to enact single loading of the specimen which is the reason for long incident and transmission bars. If the bars are too short, the stress pulses would overlap and the specimen would be subjected to successive loads. Even with sufficiently long bars, the strain gages must be installed in the proper locations far enough away from the specimen and free end of the bar to ensure strain readings don't record interfering waves. In the Split-Hopkinson Tension Bar (SHTB) in this study, it is difficult to isolate a single pulse loading. If the anvil is too short, multiple reflections within it after impact will cause multiple transmissions into the

incident bar and consequently into the specimen. If the anvil is too long, it may inhibit translation of the incident bar and restrict displacement in the specimen. For this reason, a momentum trap is sometimes used to isolate the single pulse load in the incident bar. Placed at a precise distance away, the reflected stress pulse in the anvil passes into the momentum trap when the anvil meets it. There is separation between the anvil and the momentum trap after impact and the stress pulse is contained within the momentum trap. This method however is difficult to control. The anvil poses another difficulty in that it must be rigidly attached to the incident bar. Machining an incident bar and anvil out of one continuous material is challenging and costly. Threading and welding is most commonly used, but run the risk of breaking under the extremely high loads and repeated impacts.

The most difficult problem with a SHTB in particular is gripping the specimen. Unlike the compression SHPB where the specimen is sandwiched between the transducer bars and simply supported underneath, the specimen in a SHTB must be rigidly attached to the bars. With cylindrical specimens, threading the specimen into the bars on both ends is the most common practice. This obviously requires a substantial amount of machining and is not feasible for all materials. Other methods that have been employed are wedge grips, shoulder grips, and bolting. In each of these methods it is important to ensure there is a smooth load transfer through the grip into the specimen. Pre-tensioning can be used to prevent slack in the system. The more complicated the gripping system, the greater possibility of distorting the stress wave passing through.

2.2 SHTB Construction

The SHTB at Michigan State University's Composite Vehicle Research Center is shown in **Figure 11**. This section will describe the various components designed for this specific test configuration. A more general overview of the theory and test methodology of the SHTB is outlined in **Chapter 1.5**, "Impact Test Methods: Split-Hopkinson Pressure Bar Theory."

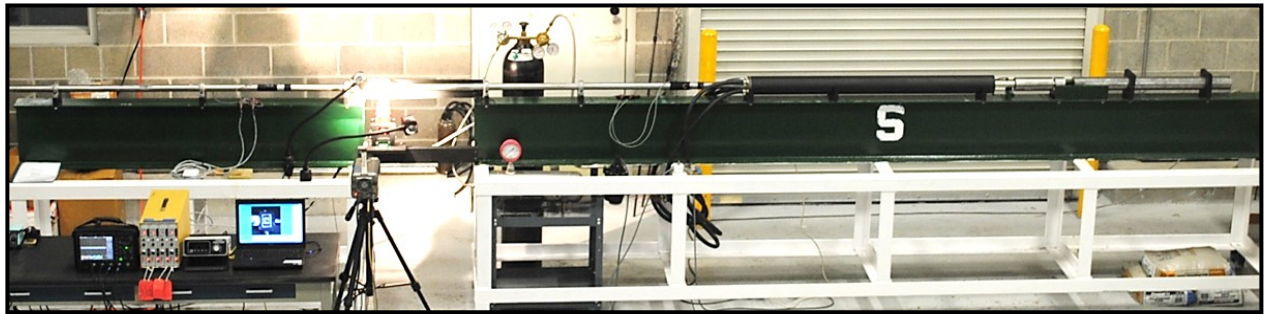


Figure 11: Tensile SHPB at Composite Vehicle Research Center, MSU.

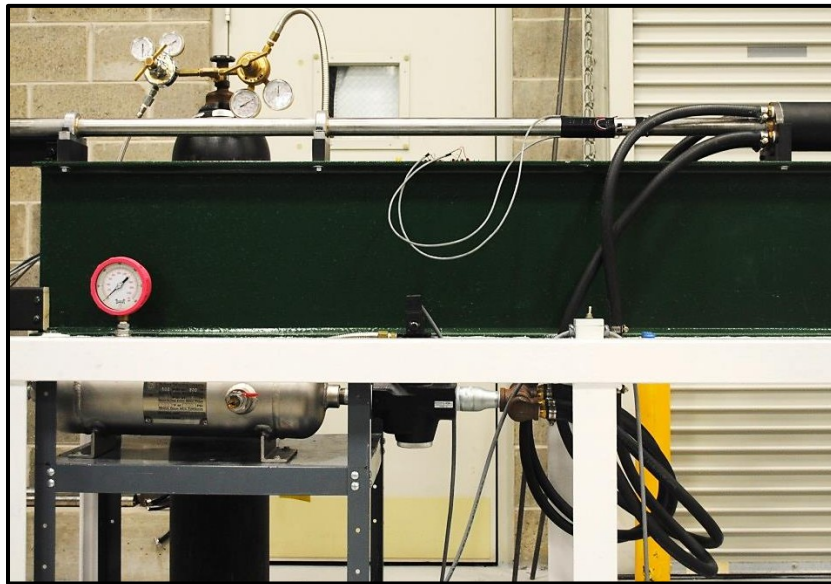


Figure 12: Compressed nitrogen gas delivery system.

The incident and transmission bars are 1.5 inch diameter 304 stainless steel bars, 12 feet and 6 feet in length respectively. They were chosen for their high strength and elastic properties and are sufficiently long enough to accommodate a 2 foot long stress pulse without pulse overlap. **Figure 12** highlights the gas delivery system employed to accelerate the striker down

the incident bar to the anvil. It is comprised of a 304 cubic foot compressed nitrogen gas cylinder, a 300 psi charge flask, and a 2 inch solenoid-actuated poppet valve and trigger. The power supply for the solenoid valve is electrically isolated from the data acquisition system power supplies to prevent voltage spikes that prematurely trigger data acquisition. 50 psi of compressed nitrogen is delivered to the 3 inch ID, 4 inch OD, 5 foot long mild steel pressure chamber via 4 EPDM rubber air hoses.

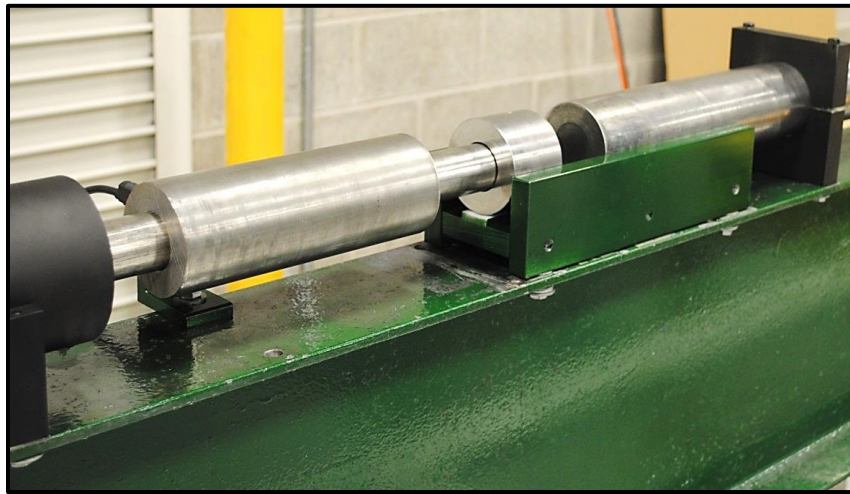


Figure 13: Impact region of SHTB showing striker, anvil, and momentum trap on Teflon PTFE track.

The 3 inch diameter, 8.5 inch long 304 stainless steel striker shown in **Figure 13** has a 1.5 inch ID bore which allows it to ride along the incident bar. The impact occurs between the striker and the 3 inch diameter, 2.25 inch long 304 stainless steel impact flange, also known as the anvil, which is threaded onto the end of the incident bar. A 3 inch by 3 inch square piece of corrugated cardboard with a 1.5 inch circular cutout is placed at the impact plane of the anvil for each experiment which functions as a pulse shaper (not shown in the figure). The selection of pulse shaper material will be discussed in **Chapter 2.3**, “System Validation.” The anvil rides on a low friction Teflon PTFE track housed within an aluminum frame. The track allows for the linear translation of the incident bar and subsequent displacement within the specimen. It also

provides support perpendicular to the direction of motion to minimize bending in the incident bar. A 3 inch diameter, 3 foot long momentum trap rides partially on the same track as the anvil and partially on its aluminum saddles and is used both for single pulse loading of the specimen and as a stopper for the incident bar and anvil.

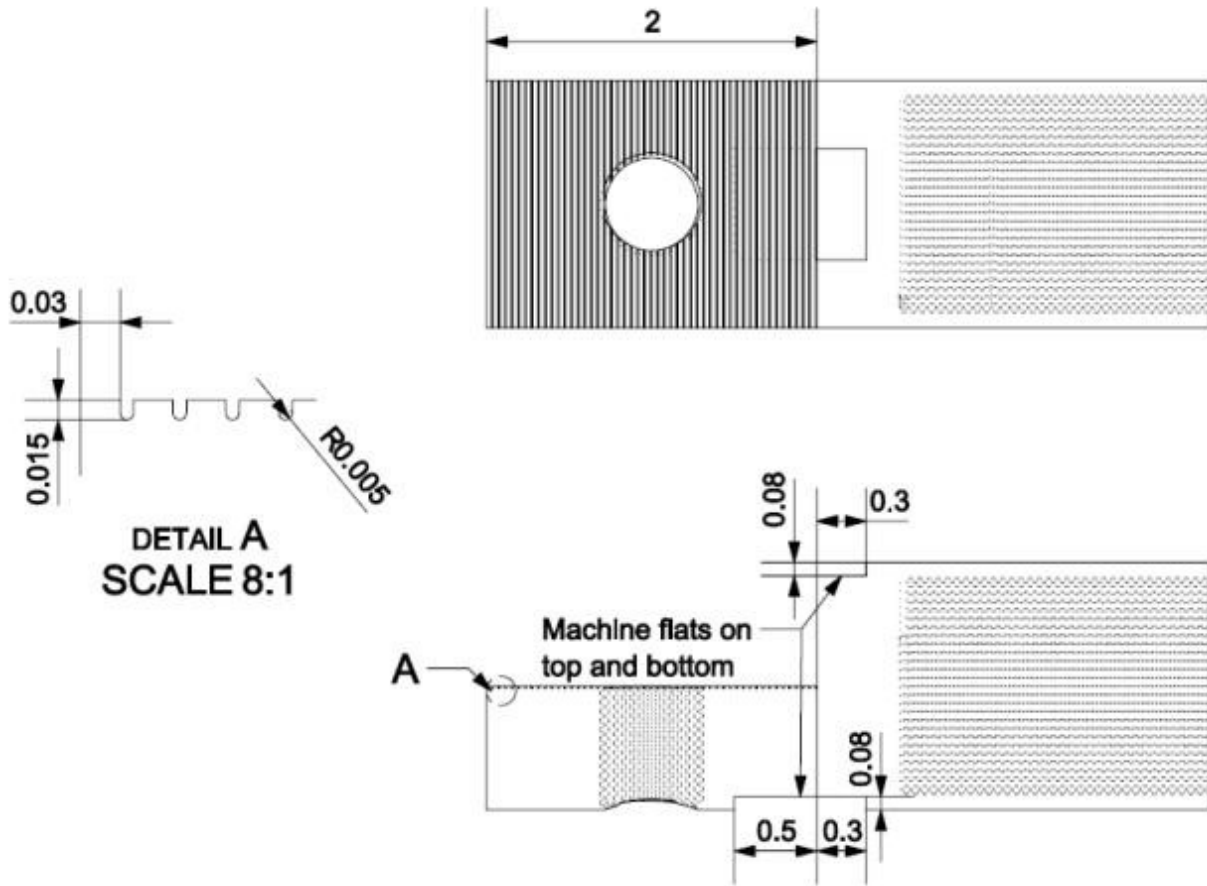


Figure 14: Schematic of specimen grip fixtures.

The custom gripping fixture used to hold the specimen is shown in **Figure 14**. It has an internally threaded bore that fixes onto the threaded end of the incident and transmission bars. With the exception of the anvil, the grips endure the most wear in the entire SHTB setup and were therefore fabricated as separate fixtures instead of directly machining onto the bars (it is easier to fabricate new fixtures rather than re-machining the bars in the event of failure). The fixtures were fabricated from the same material as the bars to reduce the impedance mismatch

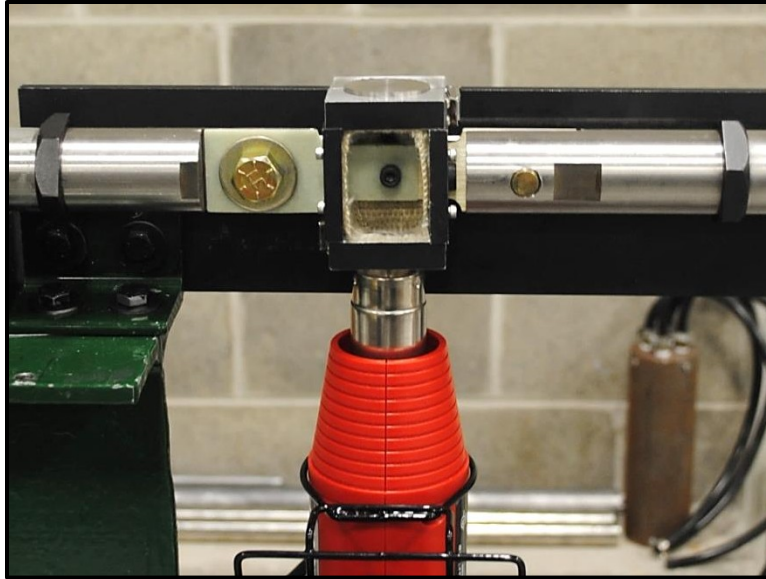


Figure 15: SHTB grip fixture assembly and temperature chamber.

between the bars and the fixtures. Serrations were machined into the grip surfaces to prevent slipping by creating a mechanical interlock between the specimen and the grip surface. This was also made possible by applying 100 ft lb of torque to the 9/16-18 x 1 inch grade 8 clamping bolts and washers. **Figure 15** shows the bar-fixture assembly with attached specimen. The black pre-tension lock nuts shown in the figure between the fixtures and transducer bars are used to tighten the fixtures against the threads of the bars, allowing for a smooth transfer of the stress pulse.

A custom convection heating chamber with ceramic fiber insulation and thermal gun heat supply for high temperature experiments is also shown in **Figure 15**. The chamber is mounted on a roller carriage which allows it to translate along with the incident bar. A more detailed model of the chamber is illustrated in **Figure 16**. The front viewing window is composed of impact-resistant borosilicate glass. There are openings in both sides that allow for the specimen to ride in and large enough to prevent contact forces. Openings in the bottom and top allow for the intake and exhaust respectively. Two pins at one diagonal ensure alignment between the two halves and two clasps along the other diagonal provide a tight seal to minimize thermal losses.

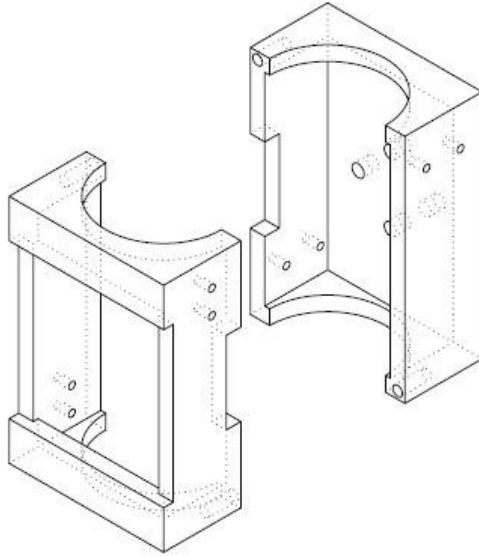


Figure 16: Exploded view model of temperature chamber for SHTB.

Two sets of diametrically opposed strain gauges (EP-08-125AD-120) shown in **Figure 17** are adhered to the transducer bars, each with a separate 3 lead-wire $\frac{1}{4}$ bridge Wheatstone circuit completed by the signal conditioning amplifier. The strain gauges measure the strain history of the loading event. From Hooke's law for linearly elastic materials, the force in both the incident and transmission bars are calculated as functions of cross-sectional area, young's modulus, and strain given by

$$F_{bar} = A_{bar}E_{bar}\epsilon_{bar} \quad (2.1)$$

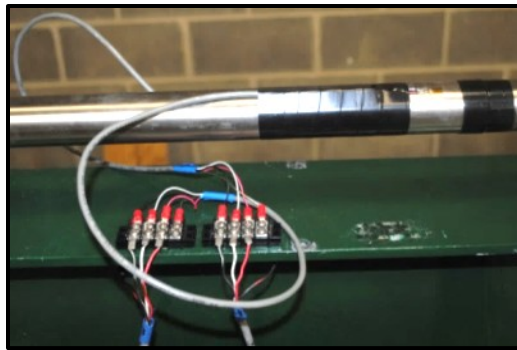


Figure 17: Diametrically opposed resistance strain gauges in 3 lead-wire $\frac{1}{4}$ bridge Wheatstone circuit configurations in incident bar.

The strain is calculated as the voltage output from the strain gauge multiplied by the calibration factor given by the signal amplifier. Along with the circular cross-sectional area of the bar, the equation becomes

$$F_{bar} = (\pi R_{bar}^2) E_{bar} (V_{sg} C) \quad (2.2)$$

The output signal from the strain gauge is amplified by the Vishay 2310B signal conditioning amplifier shown in **Figure 18** (center). A 4-channel Lecroy WaveJet 354A digital oscilloscope records the strain history in the form of voltage outputs in a .csv file for data analysis. The signals from each pair of diametrically opposed strain gages are averaged together to cancel out bending and record only the axial strain in each bar. For the present investigation, the oscilloscope was set to capture 500 data points for each channel, recording one data point at 4 μ s intervals over a 2 ms time span. The data acquisition system also includes a 10-channel Omega MDSSi8 benchtop indicator with glass braided J-type thermocouples for measuring temperature with an accuracy of $\pm 0.1^\circ\text{C}$ for temperature experiments.



Figure 18: SHTB data acquisition system including 4-channel Lecroy WaveJet 354A digital oscilloscope, Vishay 2310B signal conditioning amplifiers (4), and 10-channel Omega MDSSi8 benchtop indicator (left to right).

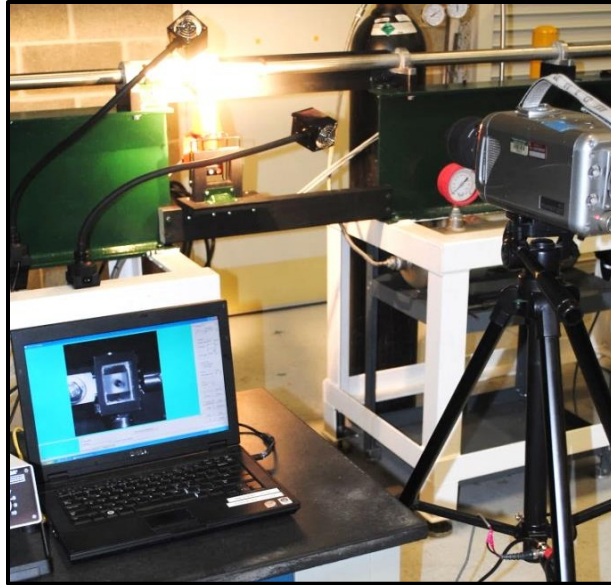


Figure 19: SHTB high speed imaging system including Vision Research Phantom V12.0 high-speed camera and Phantom camera control software

In addition to capturing strain data, the data acquisition system also includes high speed image and video recording with a Vision Research Phantom V12.0 high-speed camera shown in **Figure 19** using Phantom camera control software. The high speed camera is capable of capturing 1 million pictures per second at low resolution and was used in this study at rates of 125,000 and 250,000 images per second. Concentrated lighting was provided by two Northstar tungsten-halogen lamps.

Data-image correlation was made possible by an Eaton comet series photoelectric

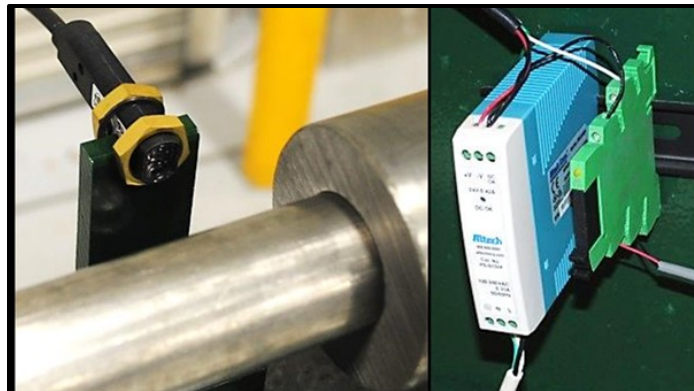


Figure 20: SHTB laser triggering system including Eaton comet series photoelectric sensor (left) along with Altech 24VDC power supply and Phoenix Contact optocoupler (right)

sensor powered by an Altech 24VDC 0.24A power supply as shown in **Figure 20**. A Phoenix Contact optocoupler was used to optically couple the laser sensor to the data and image trigger loop powered by the 10 V high speed camera power supply. The result is a simultaneous triggering of both the high speed camera and the oscilloscope. Due to the resolution limitations of the high speed camera, only one image was taken for every two strain data points.

2.3 System Validation

As previously stated, it is important to configure the SHTB in such a manner that the specimen is loaded with a single stress pulse and that the resistance strain gages are able to measure the incident, reflected, and transmission signals without interference. **Figure 9** in **Chapter 1.5**, “Impact Test Methods: Split-Hopkinson Pressure Bar Theory” illustrated a general Lagrange diagram with a subsequent explanation of wave mechanics. In order to verify that the recorded strain history is a result of the intended single pulse loading, a Lagrange diagram is needed for the current set up. **Figure 21** depicts this Lagrange diagram along with a scaled model of the actual set up for reference. Distance along the bar is shown on the x-axis with the impact plane marking the 0 reference point. The y-axis marks the time scale starting with the impact event. RSG 1 and 2 are the resistance strain gages on the incident and transmission bars respectively with orange dotted lines representing their position on the diagram while the black dotted lines represent the bar-specimen interfaces.

The light orange lines at the origin of the Lagrange diagram show the stress pulse that is created by the striker after impact. The time duration of the stress pulse created from the impact, t_{wave} , is a function of the striker’s length, l_{str} , and wavespeed, c_{str} , given by

$$t_{wave} = \frac{2l_{str}}{c_{str}} \approx 88\mu s \quad (2.3)$$

After impact, the pulse transmits into the anvil as a compression stress pulse, reflects at the free end, and transmits into the incident bar as a tensile stress pulse. The slope of the lines representing stress waves in the Lagrange diagram is equal to the material's wavespeed, which in the case of the incident and transmission bars is

$$c_{bar} = \sqrt{\frac{E_{bar}}{\rho_{bar}}} \approx 4900 \text{ m/s} \quad (2.4)$$

It can be seen in the diagram that the incident (blue), reflected (red), and transmission (purple) signals are recorded by the strain gauges without pulse interference due to the relatively short

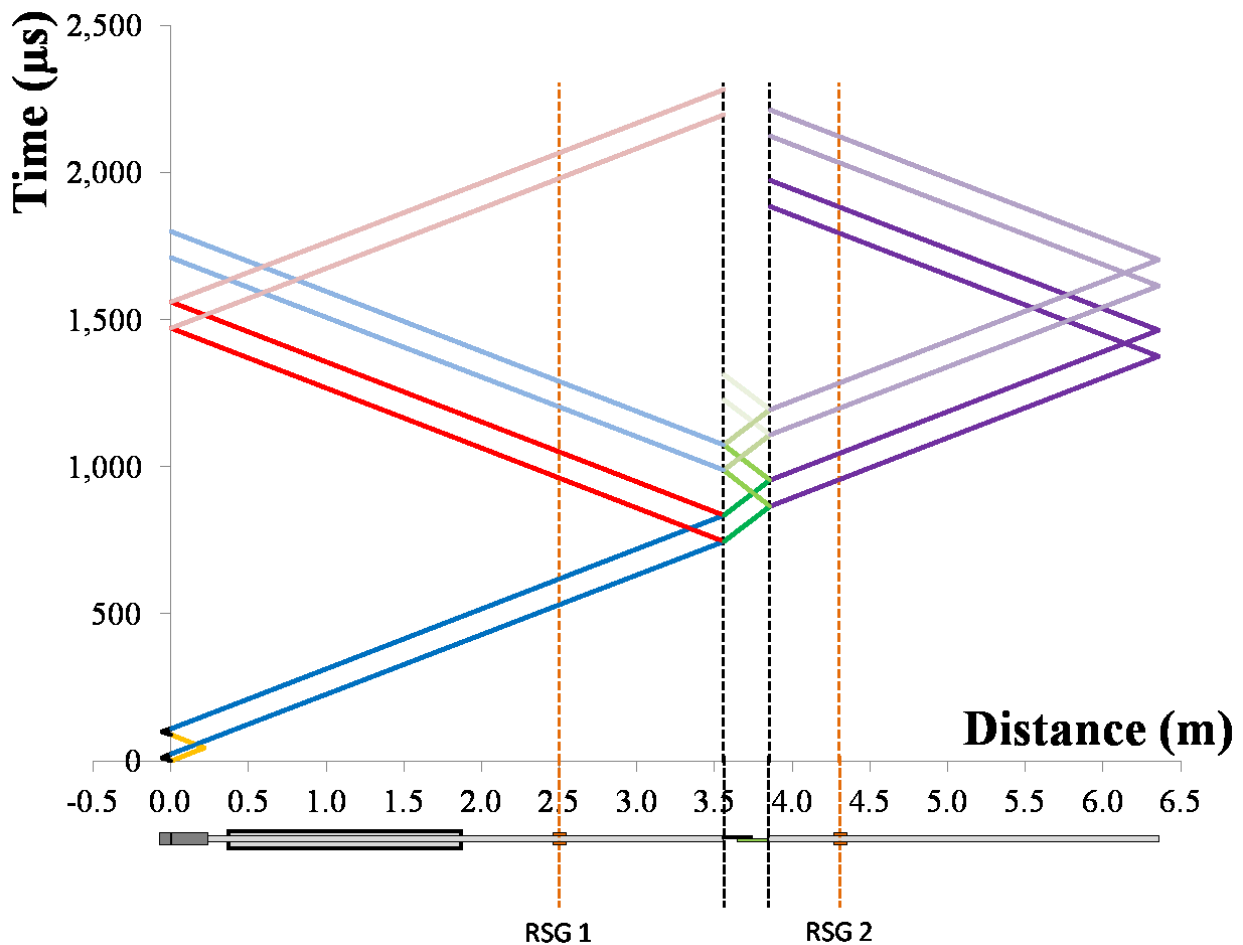


Figure 21: Scaled model of SHTB set-up and corresponding Lagrange diagram.

pulse duration in comparison to the length of the bar and the distance of the gages from the bar-specimen interfaces. Since the specimens failed during the initial loading, it is certain that the single pulse loading was achieved since the time it takes for the second loading to reflect within the bars exceeds the time of the loading event.

In addition to the isolation of the stress pulses and their successful recording via strain gages, the shapes of the stress pulses are also important. It was previously stated that shorter stress pulses with sharper rise times cause greater wave dispersion within the bars due to the high frequency of the wave, a phenomena that must be avoided or else mitigated in the one dimensional application of the stress pulse. These sharp rise times however are the result of the striker-anvil impact when no pulse shaping is used. When a deformable material (pulse shaper) is placed between the striker and anvil, the resultant pulse has a longer rise time, wider pulse width, and consequently lower dispersion (not to mention lower force amplitude which may or may not affect the ability of the load to fully fracture the specimen). Pulse shaping materials can also aid in achieving a constant strain rate [26] throughout the loading event. Selecting the correct pulse shaper has historically been done on a trial and error basis. Limited research has been published on pulse shaping [26–29], with several attempts to develop analytical and numerical models to predict the resultant stress pulse profiles. Such models are generally limited to specific pulse shaping materials and test specimens and not applicable to the current investigation. Using the historically proven trial and error approach, the following pulse shaping materials were tested: copper, polyurethane, latex rubber, paper tissue, and corrugated cardboard. The latter material produced stress pulses suitable to proceed with testing.

Validation of the auxiliary temperature chamber was performed to ensure that a uniform, stable temperature distribution was achieved in the specimen and that the transducer bars were not significantly heated so as to distort strain gage measurements. The former test was performed with 4 J-type thermocouples. **Figure 22** shows the experimental set-up with thermocouple locations. Trial tests were performed monitoring the 4 thermocouples to determine whether or not the specimen, specifically the overlap area, reached the input temperature (80°C). **Figure 23** shows the results of the trial test, confirming an average temperature of $78.7^{\circ}\text{C} \pm 0.1^{\circ}\text{C}$ for all 3

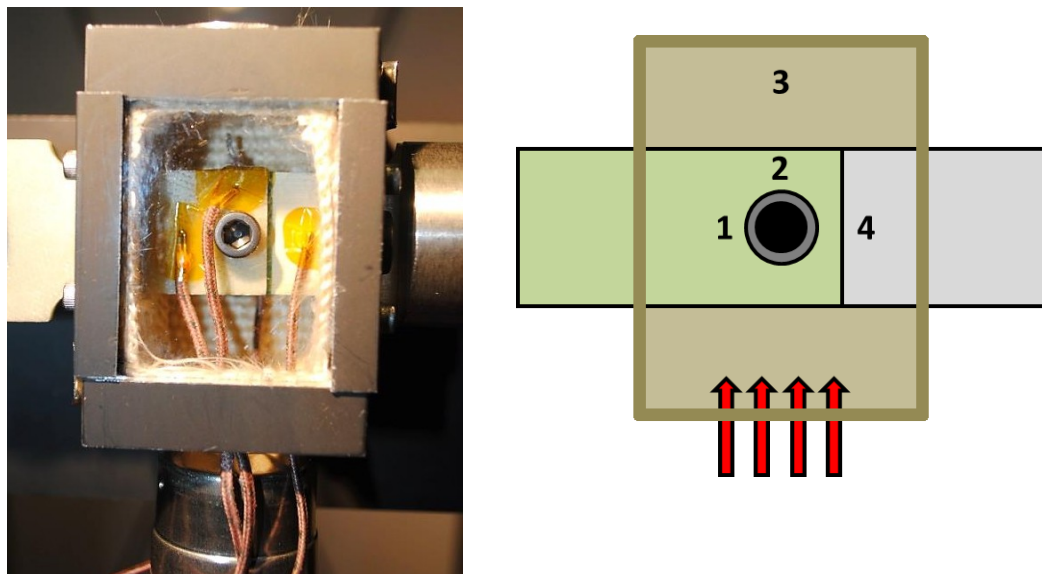


Figure 22: Temperature chamber with 4 thermocouples (left) and diagram with thermocouple locations (right).

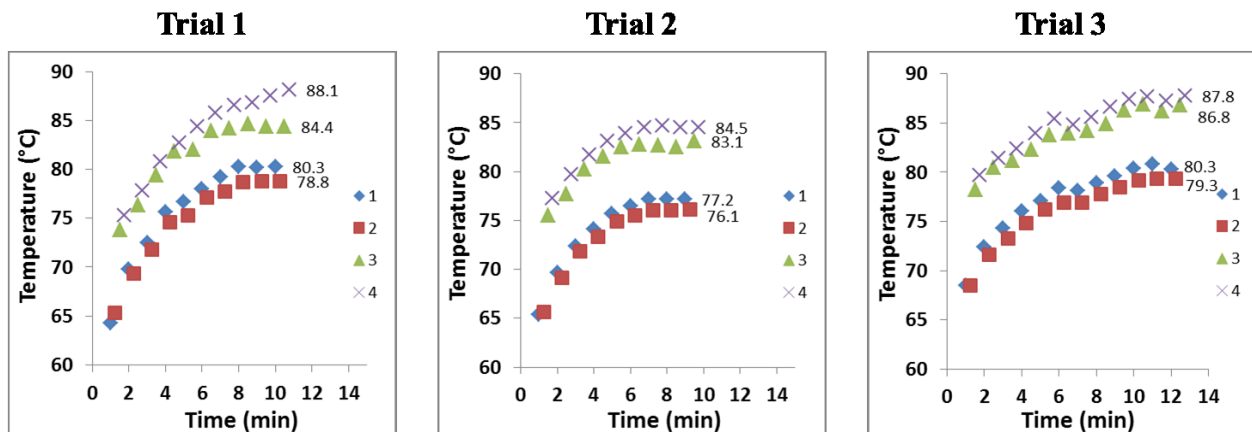


Figure 23: Temperature chamber validation experiments (3) - Temperature vs. time graphs at 4 thermocouple locations.

trials which was achieved after an average time of 8.33 minutes. Due to the consistency of the trial tests and the impracticality of using the thermocouples for every specimen, tests were performed after 10 minutes of heating at the input temperature.

Figure 24 shows the thermal imaging camera results of temperature vs. image distance for the areas surrounding temperature chamber (left) and in bar (right) over a 12 minute timeframe. In both cases, significant rises in temperature were seen in the temperature chamber and the very near surrounding area. However, the very steep drop off in temperature indicates that very little thermal energy was transferred to the bar. At 1/3 the distance from the temperature chamber to the bar, only a 1.5°C rise was seen. These results provide sufficient confidence that the elevated temperatures where isolated in the chamber and that strain measurements in the bar were not distorted.

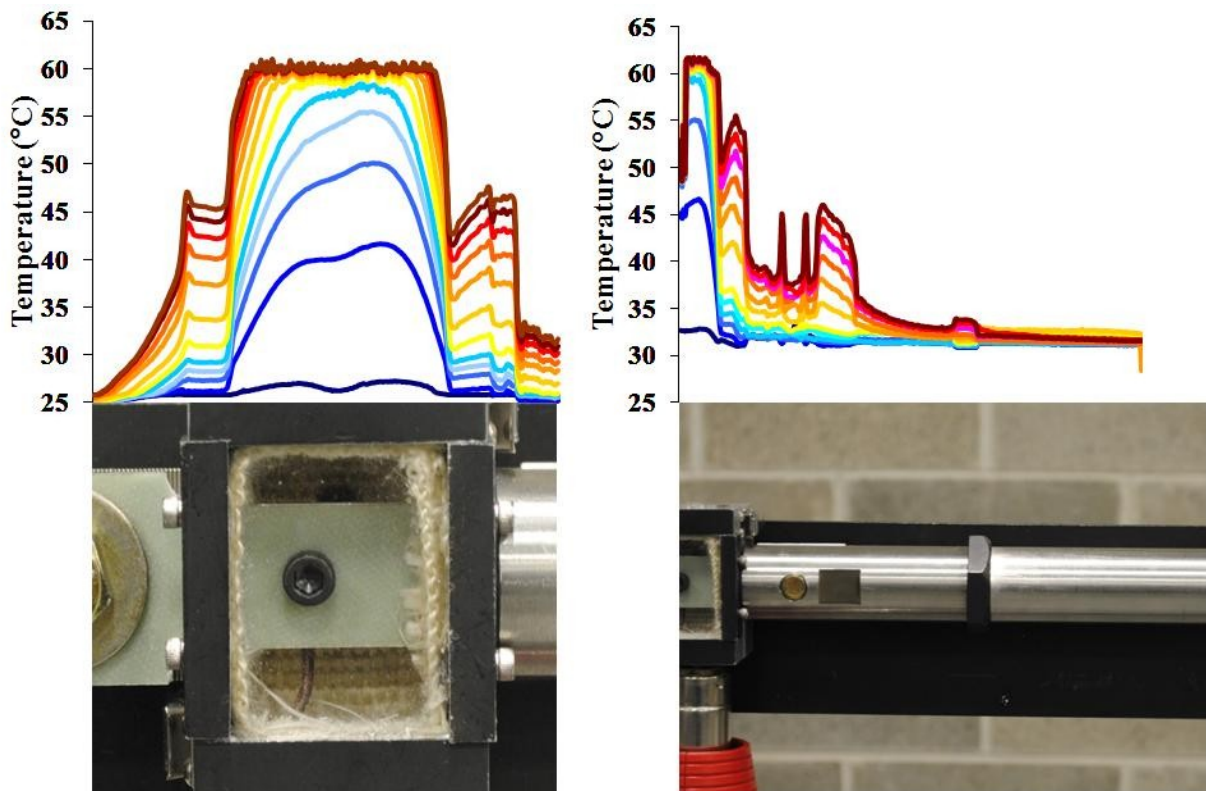


Figure 24: Thermal imaging camera results of temperature vs. image distance for area surrounding temperature chamber (left) and in bar (right) over 12 minutes.

CHAPTER 3: Mechanical Behavior of Bolted, Bonded, and Hybrid (Bolted/Bonded) Metal-Composite Joints under Impact Loading Conditions

3.1 Materials and Methods

In the first part of the investigation, static tensile testing was conducted for Aluminum/S2-glass single lap bolted, bonded, and hybrid joints in order to establish a baseline for loading rate comparison. The geometric parameters of the Aluminum 6061 T-6 materials were kept constant in all joint configurations with non-dimensional geometric ratios $d/t = 2$, $w/d = 4$, and $e/d = 2$ where d is the bolt hole diameter, t is the specimen thickness, w is the width, and e is the edge distance to the center of the bolt hole. The S2-glass/SC-15 resin composite materials were configured in a $[0/90/+45/-45]_4$ ply orientation with corresponding geometric ratios $d/t = 2$ and $w/d = 5$ with varying $e/d = 1, 2, 3,$ and 4 . A 0.25 in. diameter stainless steel bolt and nut with 40 in·lb bolt preload were used for bolted and hybrid joint scenarios. FM-94K film adhesive was used for bonded and hybrid specimens and oven cured per manufacturer's recommendations. The bond area was kept constant at 0.5 in. x 1 in. A minimum of three specimens were tested for each joint type and geometry configuration in the MTS 810 Material Test System shown in **Figure 25** [30] at a crosshead displacement rate of 1mm/min. The tabbed specimens shown in **Figure 26a** were hydraulically gripped with 5 MPa gripping pressure.

High loading rate tests were performed in a Split Hopkinson Pressure Bar (SHPB) in tension shown in **Chapter 2.2**, "SHTB Construction" for the same joint configurations as in the static testing. Two diametrically opposing resistance strain gauges in separate $\frac{1}{4}$ bridge Wheatstone circuits capture the strain history in both incident and transmission bars. The data acquisition system consists of a Vishay 2310B signal conditioning amplifier and a LeCroy Wave Jet 354A digital oscilloscope. High speed video and digital images were taken at a rate of



Figure 25: MTS 810 Material Testing System used for static testing at 1 mm/min crosshead displacement.

125,000 frames per second using a Phantom V12.0 high speed camera which was synchronized with the oscilloscope via a laser triggering system for data-image correlation. A minimum of four specimens, modeled in **Figure 26b**, were tested for each joint type and geometry configuration. Failure mode and joint strength comparisons were made between the bolted, bonded, and hybrid joints at static and high loading rates.

In the second part of the investigation, the effect of materials and surface preparation at high loading rates was considered for comparison against the Aluminum/S2-glass bolted and hybrid joints in the first study. The effect of alternative composite materials on mechanical behavior was studied for Aluminum/E-glass single-lap bolted and hybrid joints tested in the SHTB for $e/d = 1$ and 4. The E-glass/epoxy composite panels were made from a G10/FR4 weave with $[0/90]_{16}$ ply orientation. Next, the effect of alternative metal materials on mechanical behavior was studied for Advanced High Strength Steel (AHSS)/S2-glass single-lap joints for bolted joint $e/d = 1-4$ and hybrid joint $e/d = 1$ and 2. The effect of surface preparation on the Aluminum/S2-glass and AHSS/S2-glass hybrid joints were considered for $e/d = 1$ and 2.

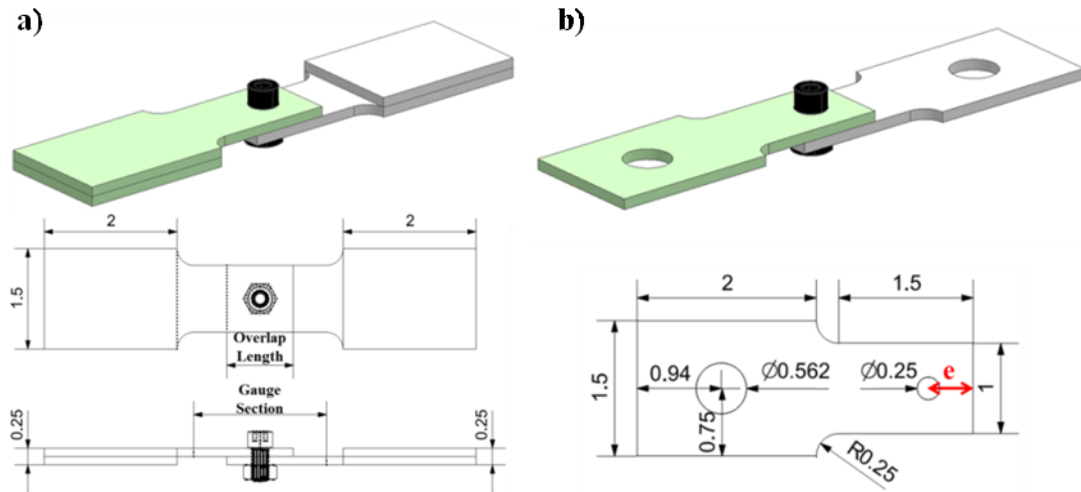


Figure 26: Models and schematics with dimensions of single-lap a) static specimens and b) SHTB specimens.

Aluminum surfaces were prepared by phosphoric acid anodizing per ASTM D3933-98. The AHSS surfaces were prepared by surface etching per ASTM D2651-01. Both aluminum and AHSS specimens were coated with BR127 corrosion inhibiting primer. Lastly, the mechanical behavior of Aluminum/S2-glass bolted and hybrid joints was evaluated at 80°C for $e/d = 1$ and 4 and compared against room temperature.

3.2 Joint Behavior under Static Loading

Static loading was conducted for the Aluminum/S2-glass single lap bolted and hybrid joints, e/d 1-4, and bonded joints shown in **Figure 27** in order to establish a baseline for loading rate comparison. This subchapter will address bolted, bonded, and hybrid joints individually for both their mechanical response to tensile loading and the failure modes experienced by each. **Figure 28** illustrates a typical load-displacement curve of a bolted single-lap joint with $e/d = 1$. The behavior can be divided into four distinct regions: Initial Loading, Joint Slip, Post-slip Loading, and Unloading. In the initial loading region, the joint exhibits linearly elastic behavior as the applied load is transferred through the frictional contact created by the bolt preload, both

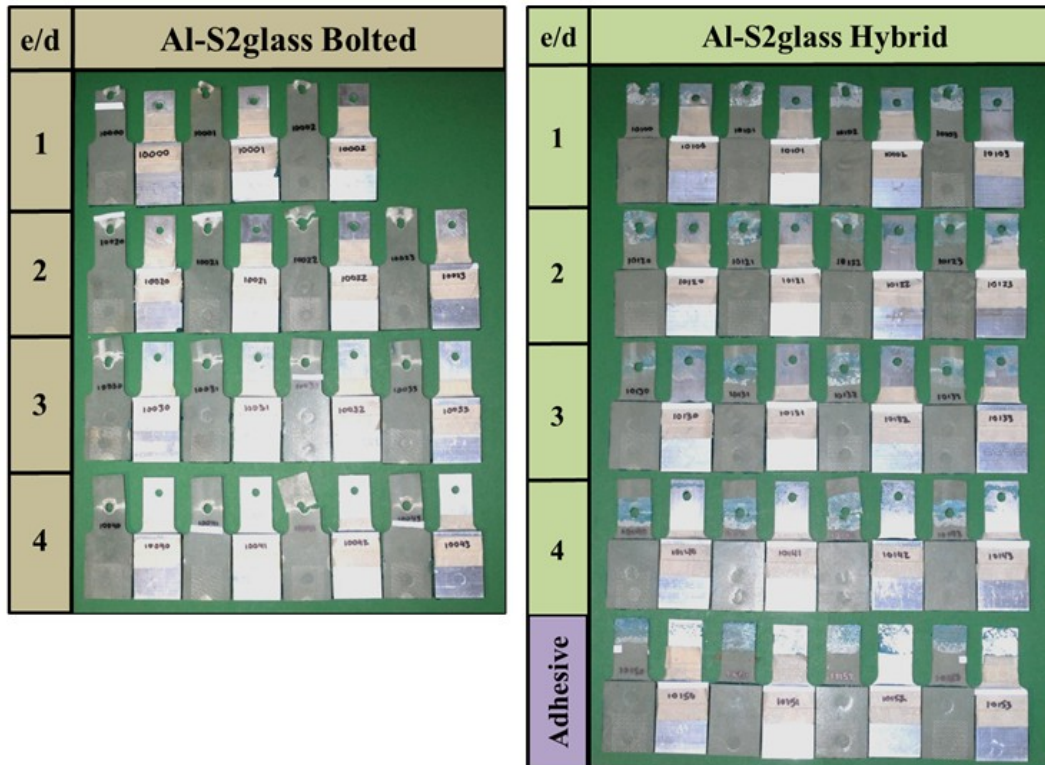


Figure 27: Aluminum/S2-glass single-lap joints tested statically in a MTS 810 system.

between the contact surfaces of the bolt head and nut with their respective contact materials, and between the materials themselves. Once the applied load overcomes preload friction, the materials slip relative to one another due to the clearance between the bolt and the bolt hole, marking the joint slip region. When contact is made between the bolt shank and the bearing surfaces of the bolt hole, the post-slip region begins as well as the initiation of damage within the material. Load increases within the joint until ultimate stress, after which residual load bearing capacity is observed to fracture in the unloading region.

Figure 29 shows deformation curves for bolted joints for varying e/d ratios. The initial loading and joint slip regions prove to be invariant with respect to bolt hole edge distance. Conversely, joint strength is proportional to and dependent on edge distance and approaches an asymptotic region between $e/d=3$ and $e/d=4$. Fracture displacement is also proportional to edge distance.

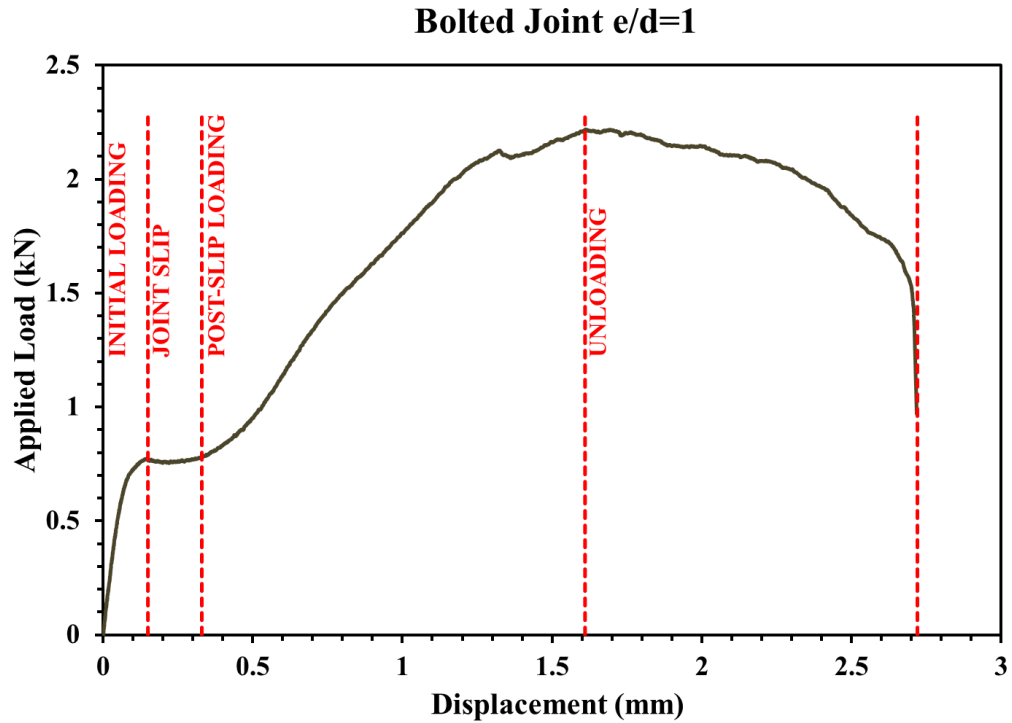


Figure 28: Load-displacement curve for bolted single-lap joint, $e/d=1$.

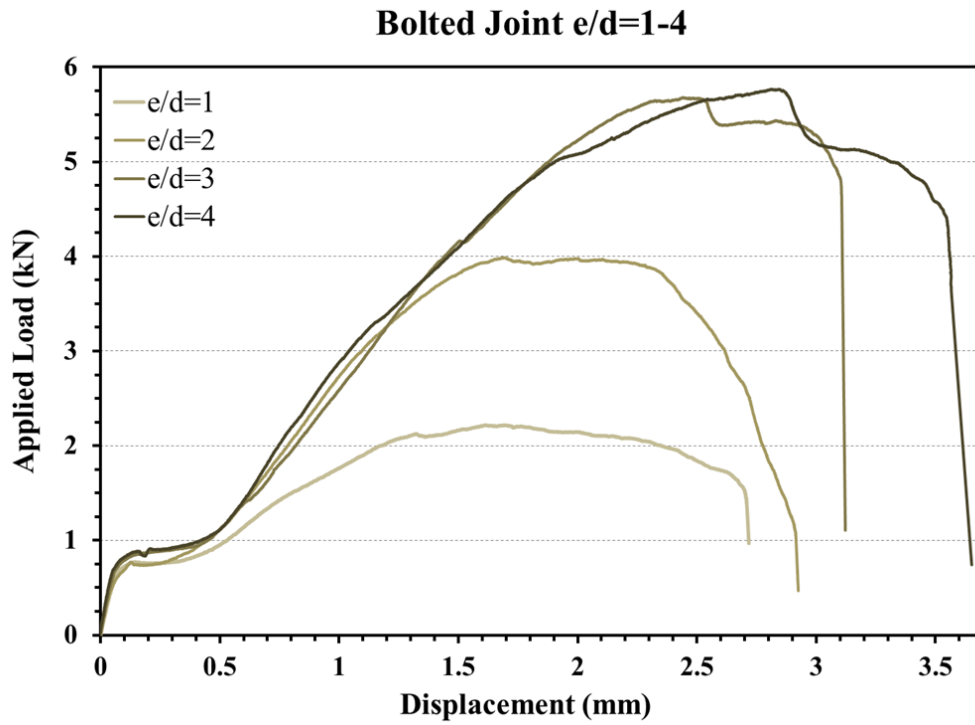


Figure 29: Load-displacement curves for bolted single-lap joints, $e/d=1-4$.

In addition to load behavior, failure mode is an important component of mechanical response often used in design considerations. **Figure 30** illustrates three of the most common modes of failure in filled hole plates, the geometric planes that affect them, and the mathematical equations used in determining failure [9]. As shown in the figure, the modes of failure in bolted joints are highly dependent on the geometry and material properties of the material. The below model demonstrates the reason why reducing w/d below a certain threshold results in net tension failure, since width is inversely proportional to the stress developing within the plate for the net tension failure mode only. Similarly, reducing e/d below a certain threshold results in shear out failure since edge distance is inversely proportional to the stress developing within the plate for the shear out failure mode only. In both instances, sufficiently large width and edge distance makes only bearing failure mode possible, a function only of the applied load, bolt hole diameter, and plate thickness.

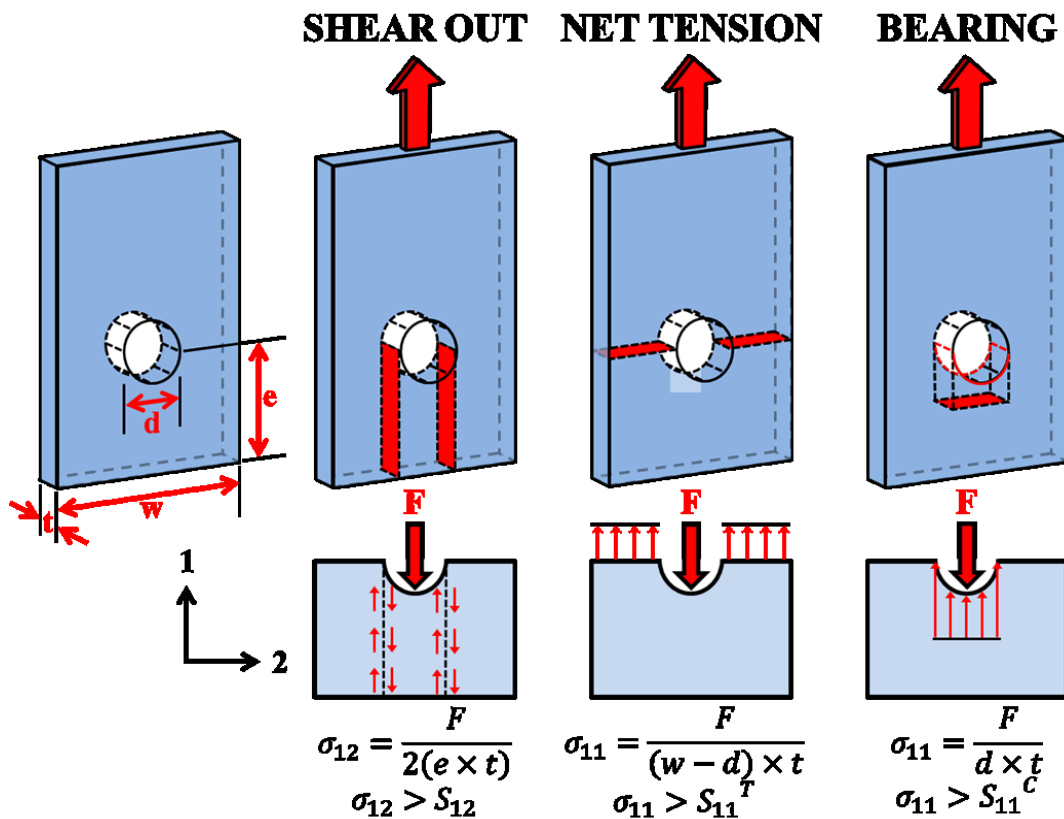


Figure 30: Common failure modes for bolted assemblies and representative equations. [9]

and material thickness. This is why bearing mode is considered the strongest mode of failure and also the most desired in design considerations.

Observed failure modes for varying e/d ratios are shown in **Figure 31**. The bolted joint at $e/d=1$ demonstrates shear out failure which is considered to be the weakest mode of failure, not only as a function of lower ultimate strength, but also due to its catastrophic nature where there is no post fracture load bearing capacity. Shear out failure initiates at the highest stress concentration within the material, generally at the bolt hole location perpendicular to the loading direction. On the opposite end, bolted joints at $e/d=3$ and 4 exhibit bearing mode of failure which is considered the strongest failure mode, not only as a function of higher ultimate strength, but also due to its progressive nature which permits post fracture load bearing capacity. Bearing failure is a result of fiber crushing in the compressive region in front of the bolt shank as shown in **Figure 30**. Since there is some net tension failure observed at $e/d =3$ and 4, it is likely that the selected width was not large enough to purely isolate the e/d variable. The similar failure modes in $e/d =3$ and 4 correspond to the similar ultimate strength and profile of both joint configurations as observed in **Figure 29**.

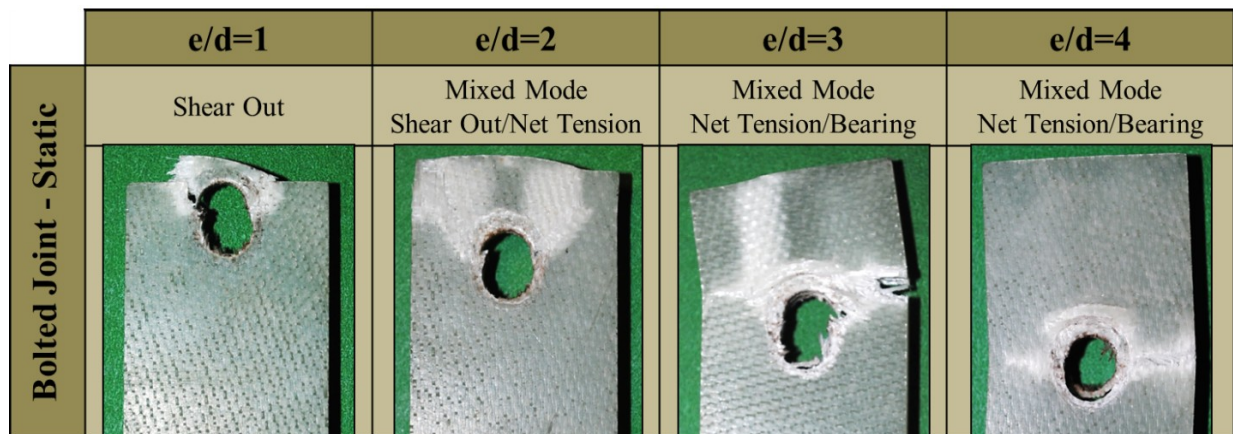


Figure 31: Observed failure modes for Aluminum/S2-glass bolted joints, $e/d =1-4$, under static loading.

A comparison of the load-displacement behaviors of bolted joints, $e/d = 1$ and 4, and that of a bonded joint is displayed in **Figure 32**. Unlike bolted joints which exhibit four independent behavior regions, the bonded joint demonstrates nonlinear loading from initiation to ultimate failure and has no post fracture load bearing capacity. Bonded joint strength for the FM-94 structural adhesive is also notably higher than that of the bolted joints presented here, although fracture occurs at a lower displacement.

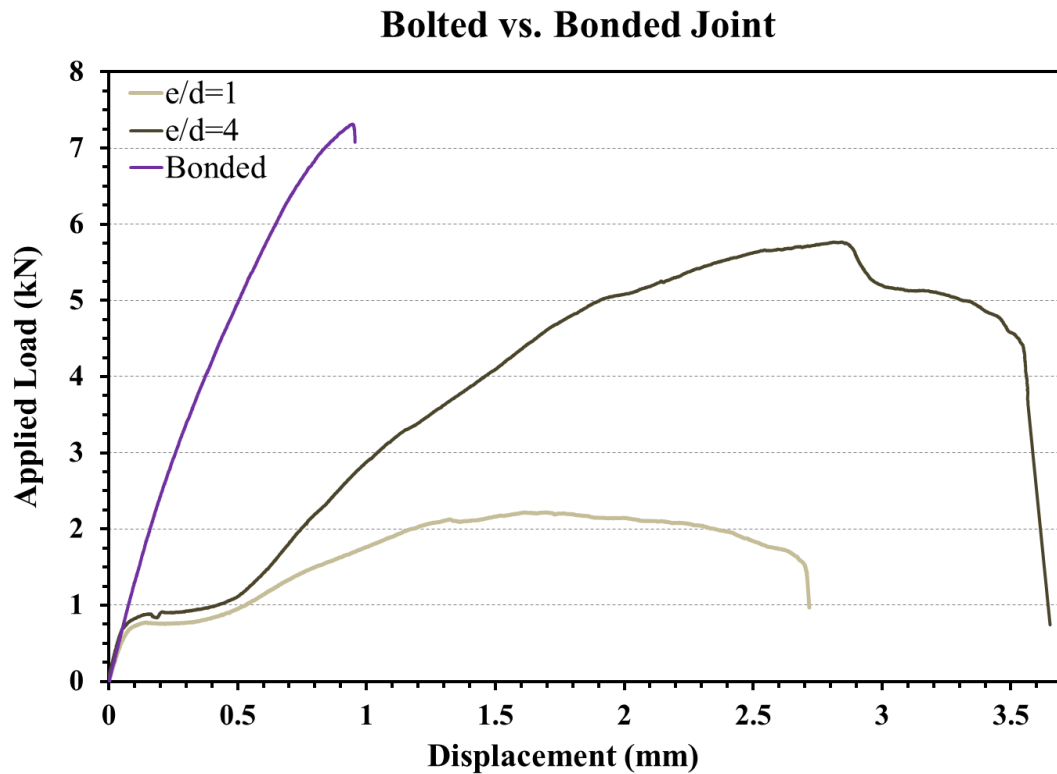


Figure 32: Load-displacement curves for bonded and bolted single-lap joints, $e/d = 1$ and 4.

There are four basic types of failure modes in bonded joints which are depicted in **Figure 33**: cohesive, adhesive, mixed, and adherend failure [31]. Cohesive failure occurs when the bonds between the adhesive and the adherend are stronger than those within the adhesive layer itself. While this is a preferred method of adhesive failure, it can also occur prematurely if the applied adhesive is too thick. Adhesive failure occurs when the adhesive separates from one of

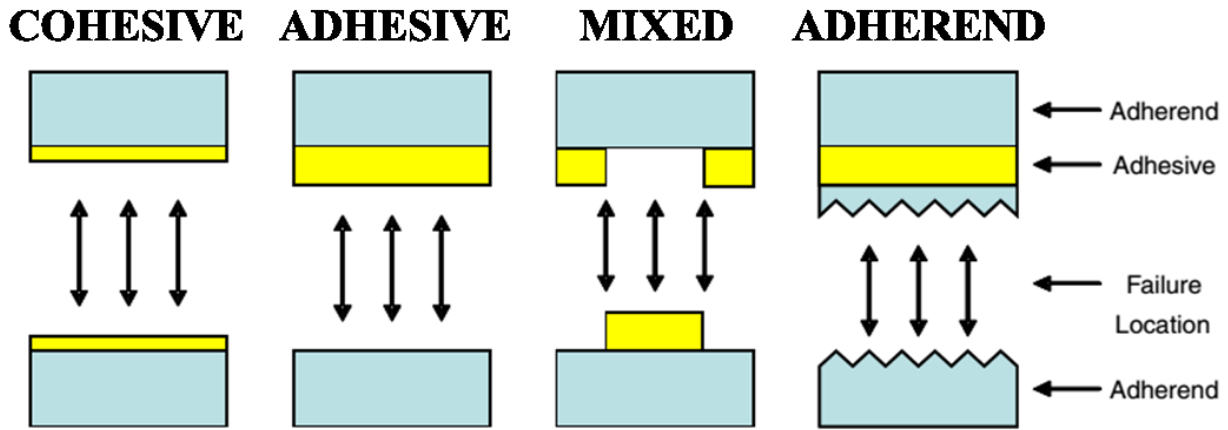


Figure 33: Common failure modes for bonded single-lap joints. [31]

the two adherends. This type of failure generally results from insufficient surface preparation on the adherend where the separation occurred, although it can occur in the case of dissimilar material adherends where the bonding affinity is greater for one of the adherends than the other. Mixed mode of failure is similar, this time with portions of adhesive-adherend interracial failure on both adherends. Lastly, adherend failure occurs when the entire adhesive system is stronger than the adherend that failed.

Observed failure modes for the bonded joints in this study are shown in **Figure 34**. All

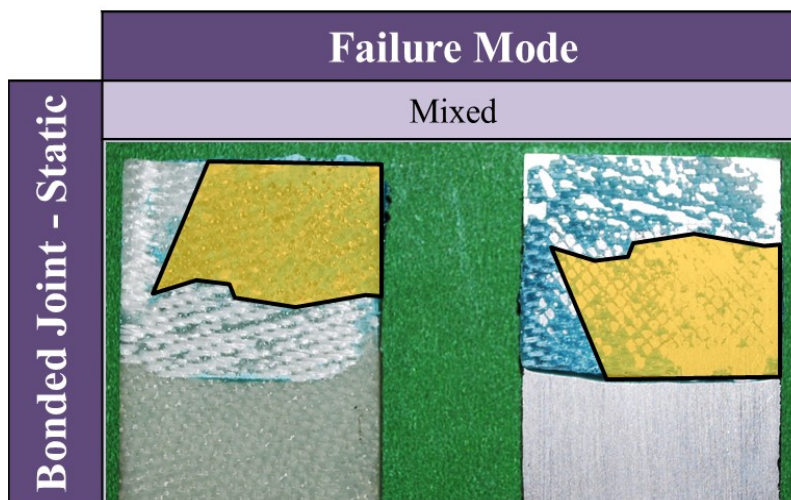


Figure 34: Observed failure modes for Aluminum/S2-glass bonded joints under static loading.

four specimens failed in mixed mode of failure. The yellow highlighted area on the left shows the adhesive that is still left intact on the composite specimen. The area on the right shows exactly the same size and shape of the missing adhesive on the aluminum plate. As previously mentioned, this is likely due to partially insufficient surface preparation on both adherends.

The deformation behavior of bolted, bonded, and hybrid joints are compared in **Figure 35**. Hybrid joints display similar initial loading behavior to that of bonded joints and seem to be dominated by the adhesive constituent which is the primary load-bearing member. After adhesive failure, the bolt takes up the load and imitates the same behavior as the purely bolted joint until ultimate failure. Joint slip in the hybrid joint occurs post-adhesive failure and prior to the bolt taking up the load. The hybrid joint deformation behavior can be described as the

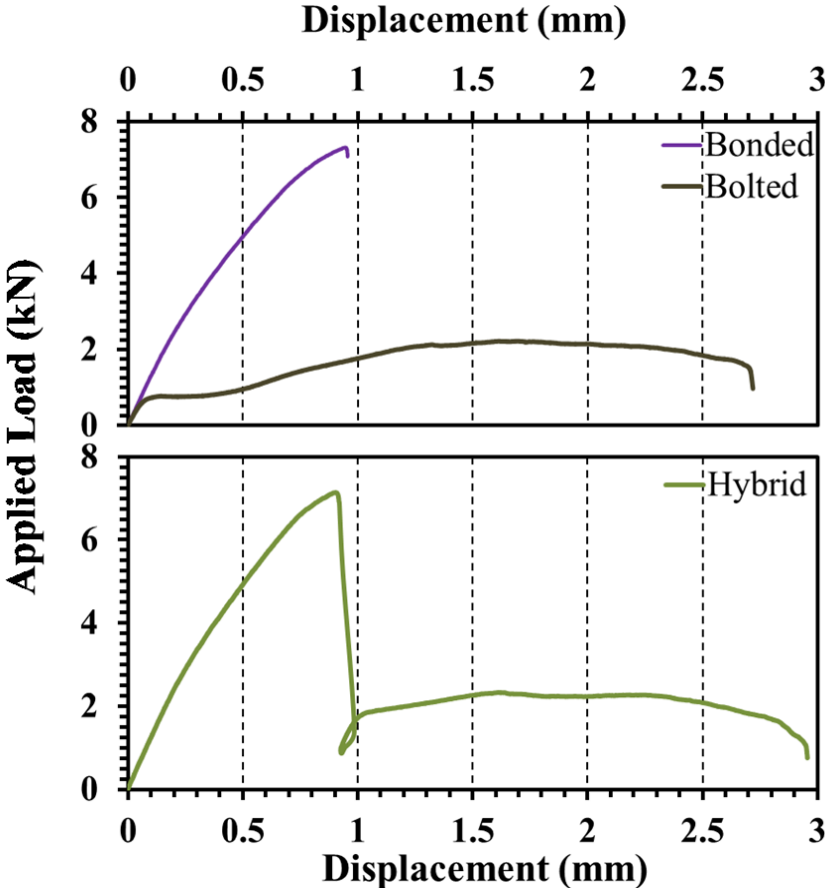


Figure 35: Load-displacement curves for bonded and bolted single-lap joints, $e/d=1$ (top), and hybrid single-lap joint, $e/d=1$ (bottom).

superposition of both bonded and bolted joint behaviors. This can be seen for each e/d ratio in **Figure 36**, where the post-adhesive failure deformation in the hybrid joint resembles the exact profile of the bolted joint, both in peak load and displacement. The overall peak load of the hybrid joint is equal to the failure load of the adhesive and is relatively equal in magnitude for all e/d ratios. From a design perspective, the hybrid joints have adopted the best properties of both the bonded and bolted joints, having the strength and uniform loading capabilities of the bonded joint during initial loading and the sustained load bearing capacity of the bolted joint after failure has initiated. **Figure 37** gives a failure mode comparison for the bolted and hybrid joints under static loading for $e/d = 1-4$. With only a slight variation at $e/d = 3$ where the hybrid joint failed only in net tension compared to the bolted joint which displayed both net tension and bearing failure modes, the failure modes at every e/d are relatively the same for both types of joints.

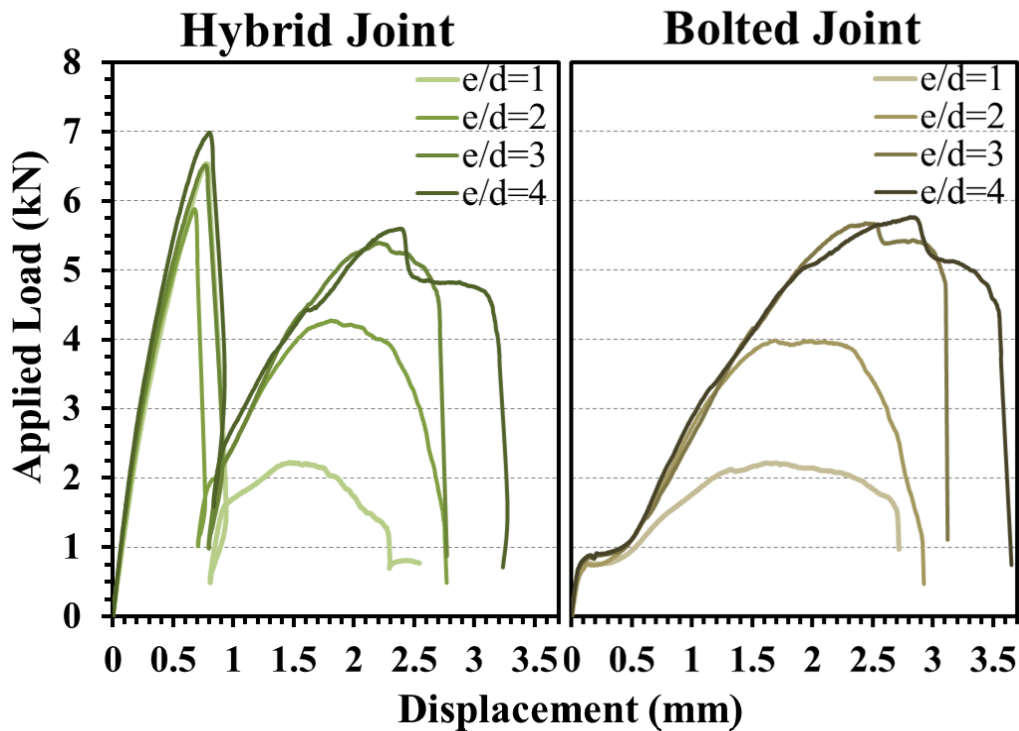


Figure 36: Load-displacement curves for hybrid single-lap joints, $e/d = 1-4$ (left) and bolted single-lap joints, $e/d = 1-4$ (right).

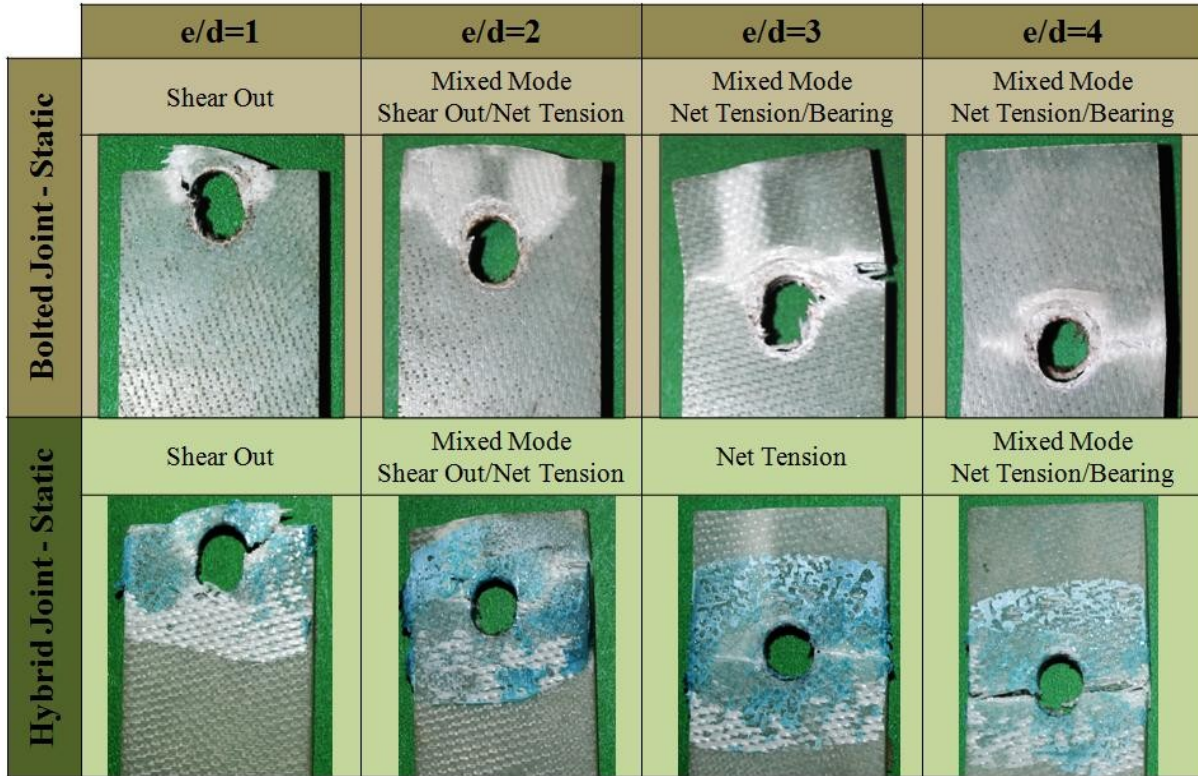


Figure 37: Observed failure modes for Aluminum/S2-glass bolted and hybrid joints, $e/d = 1-4$, under static loading.

3.3 Joint Behavior under Impact Loading

Impact loading was conducted in the SHTB for the same Aluminum/S2-glass single lap bolted, bonded, and hybrid joints as those tested statically for loading rate comparison. This subchapter will also address bolted, bonded, and hybrid joints individually for both their mechanical response to tensile loading and the failure modes experienced by each, now with comparison to their static counterparts. **Figure 38** shows the specimens tested in the impact analysis.

Aluminum/S2-glass single-lap joints exhibit vastly different behavior under impact vice static loading conditions. Several differences can be observed when comparing bolted joints under both loading scenarios as demonstrated in **Figure 39**. The graphs here are shown as functions of applied load and time as opposed to the load-displacement curves in the previous

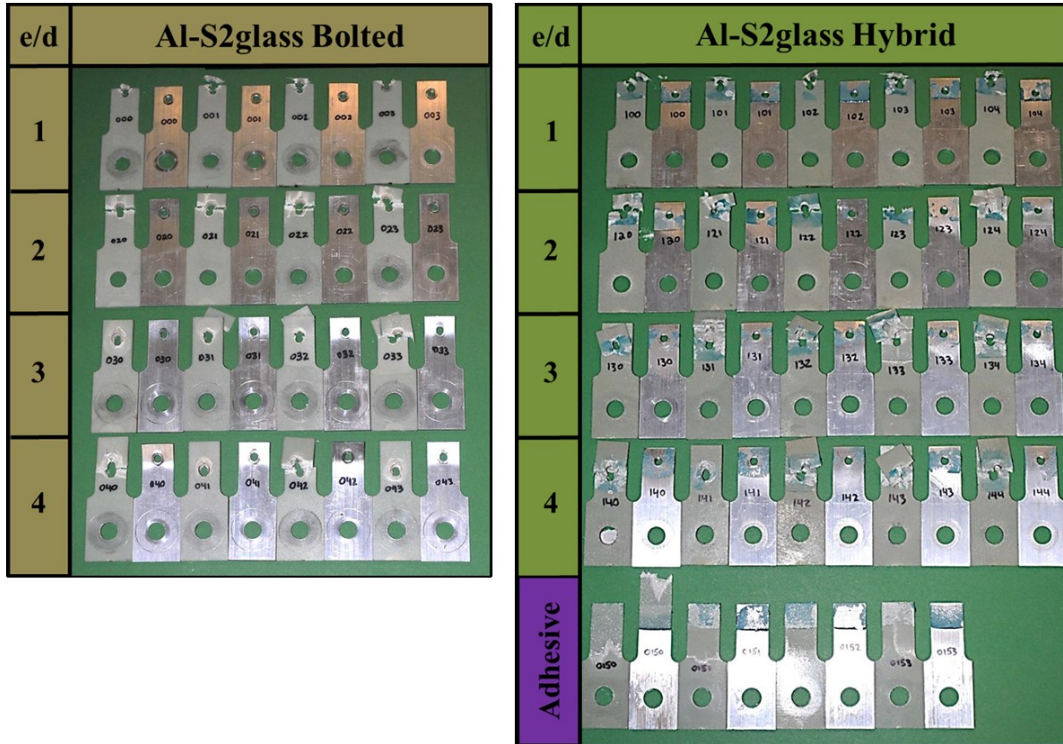
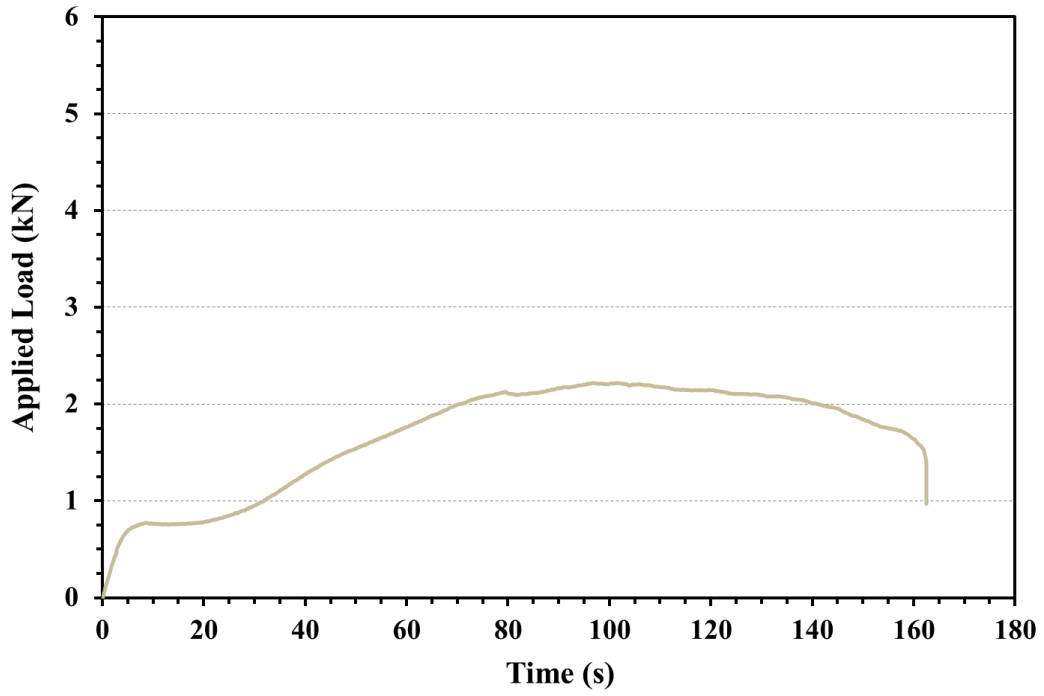


Figure 38: Aluminum/S2-glass single-lap joints tested dynamically in a SHTB.

section. This is because displacement measurements were not taken in the SHTB and in fact are not practical when testing structures since the displacement field within the specimen is not uniform. Note the time scale difference in both loading cases. The static loading event occurs over approximately 3 minutes, while the impact event occurs in less than $\frac{1}{2}$ a millisecond, approximately 350,000 times faster in the impact test than the static.

One immediate observation is that peak load is 2.6 times greater under impact loading for a bolted joint with $e/d=1$ and is in fact greater at every e/d ratio. This can be explained by material rate sensitivity as discussed in **Chapter 1.3**, “Impact Test Methods: Discussion.” Although no displacement measurements were made, it is expected that displacement will be lower in the impact case, given the higher peak load. There is also no discernible slip region in the bolted joint under impact loading. A closer look at the mechanical behavior of the impacted joint is needed to understand the differences in behavior.

Bolted Joint $e/d=1$ - Static



Bolted Joint $e/d=1$ - Impact

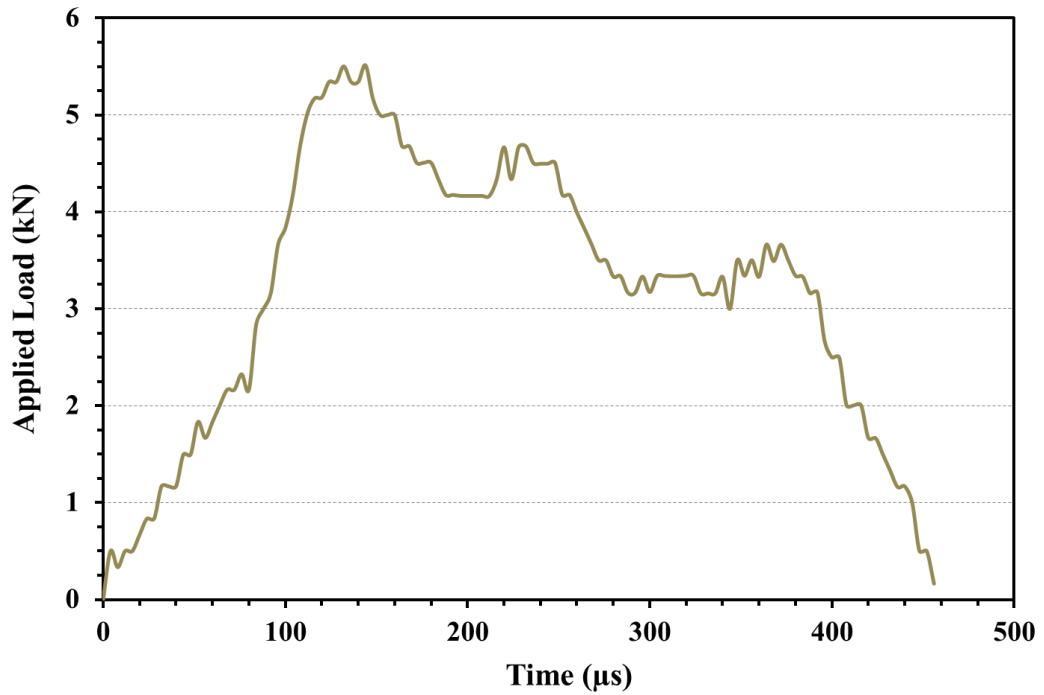


Figure 39: Load vs. time curves for bolted joint $e/d=1$ for static (top) and impact (bottom) loading conditions

Figure 40 shows the load-time curve for the bolted joint, $e/d = 1$, subjected to impact along with the high speed images of the specimen at 4 different points in the loading event. The region spanning between points 1 and 2 is the initial loading phase to peak load. As previously stated, there is no discernible slip region in the impact behavior. Different from the static case, where the applied load overcomes the preload frictional resistance after which the bolt translates until contact is made between the bolt shank and bolt hole bearing surfaces, here bolt preload friction is instantly overcome and the bolt not only translates, but also rotates through the initial loading phase. Bolt rotation in the static case only occurs after slipping. The translation and rotation in the impacted joint can be clearly seen in **Figure 41**, where translation is seen both in the vertical bolt axis and the translating edge of the lower material with respect to the upper one. In this case, the bolt experiences a 3 degree rotation. This phenomenon can be observed for both bolted and hybrid joints at every e/d ratio. Another observation made is that while composite

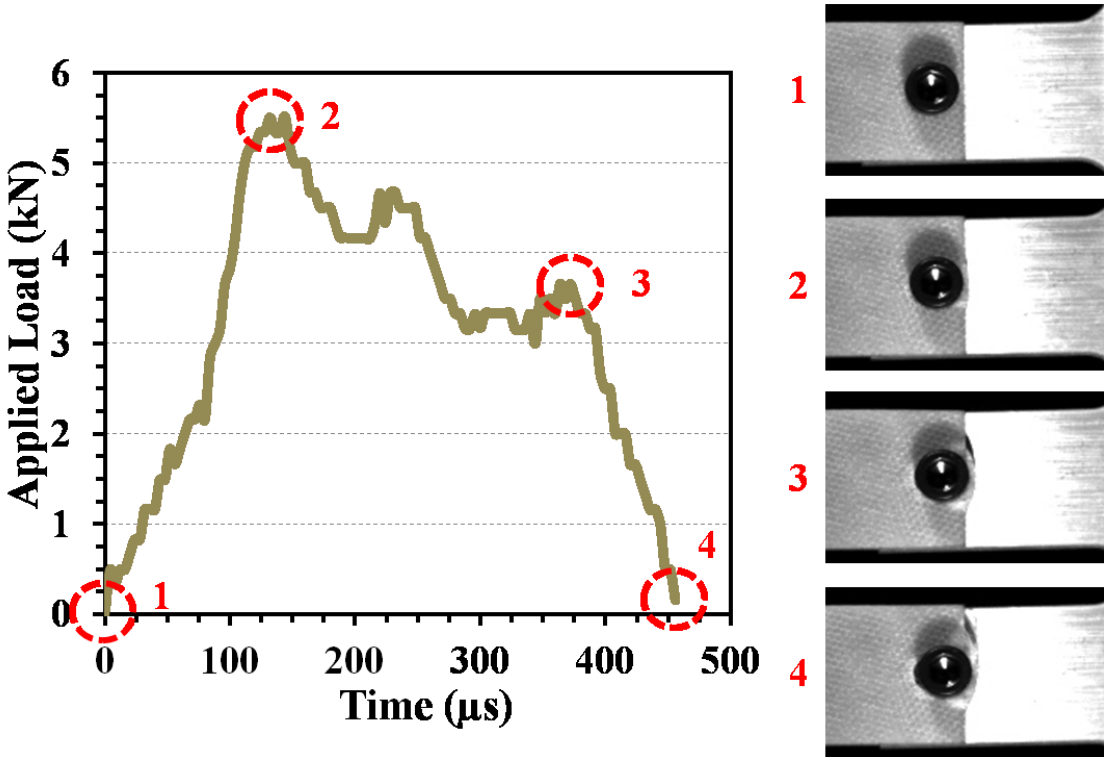


Figure 40: Load-time behavior of a bolted joint, $e/d = 1$, subjected to impact with high speed images at 4 points along the loading event.

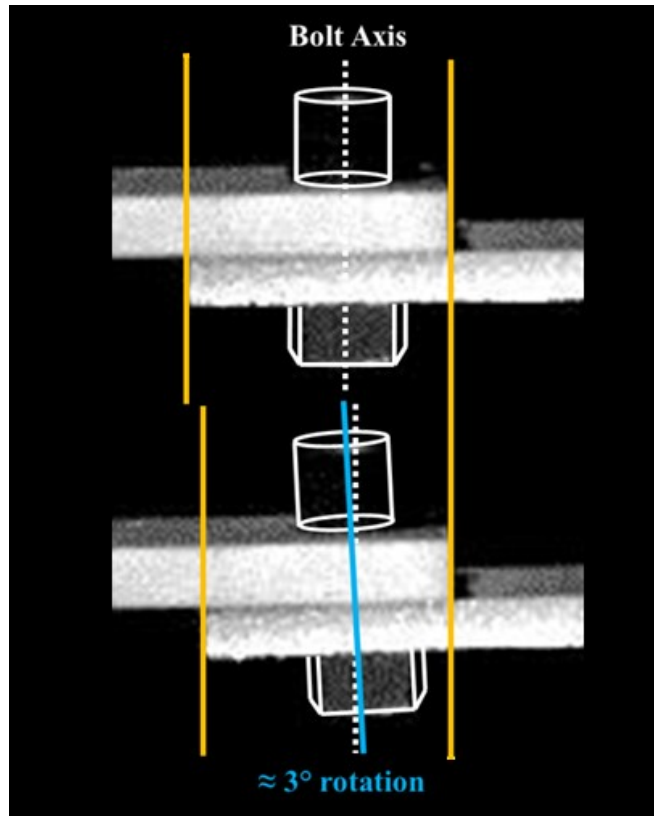


Figure 41: High speed images of joint slip and bolt rotation in bolted joint, $e/d = 1$, subjected to impact.

damage is not seen in the static case until after slip occurs, here slip and composite damage are coupled, most likely due to the rotation of the bolt in the slip region. Picture 2 in **Figure 40** illustrates the observed damage, with shear out cracks forming at the bolt hole location and extending axially to the free edge of the composite.

Failure modes also differ under impact conditions as shown in **Figure 42**. One important difference is the observable sub-surface deformation in the static scenario, where the loading time was sufficient to permit damage propagation through this compressive region. This is not the case in the impact conditions, where no sub-surface deformation is observed due to the insufficient time for molecular dislocations to develop. In both cases, damage initiates at the same location but progresses differently. Interlaminar shearing is observed in the impact case and not at all in the static. Under impact, the fiber-matrix interaction properties have more of a role in

the failure mode. There is also a slight change in overall failure mode from static to impact, where pure bearing failure is observed at $e/d=4$ under impact as opposed to a mixed mode in the static.

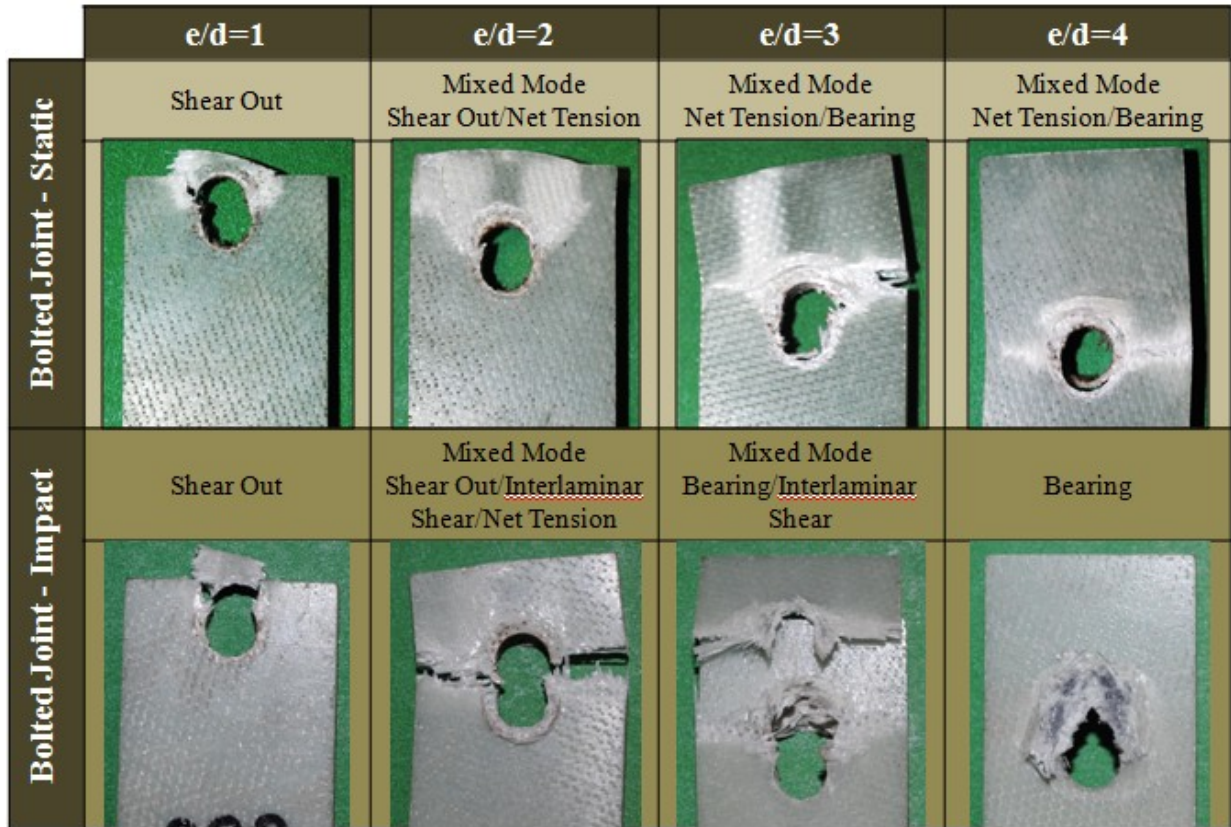


Figure 42: Observed failure modes for Aluminum/S2-glass bolted joints, $e/d=1-4$, under static and impact loading.

Bonded joints also display different behavior when subjected to impact loading. **Figure 43** illustrates the load-time curve for the bonded joint along with the high speed images of the specimen at 4 different points in the loading event. While the loading behavior in static is nonlinear throughout the entire event, the impact behavior is more linear in nature. Additionally, the load in the impacted bonded joint returns back to 0 after the peak load, whereas the loading event is complete after reaching the peak load in the static case. One reason for this is the

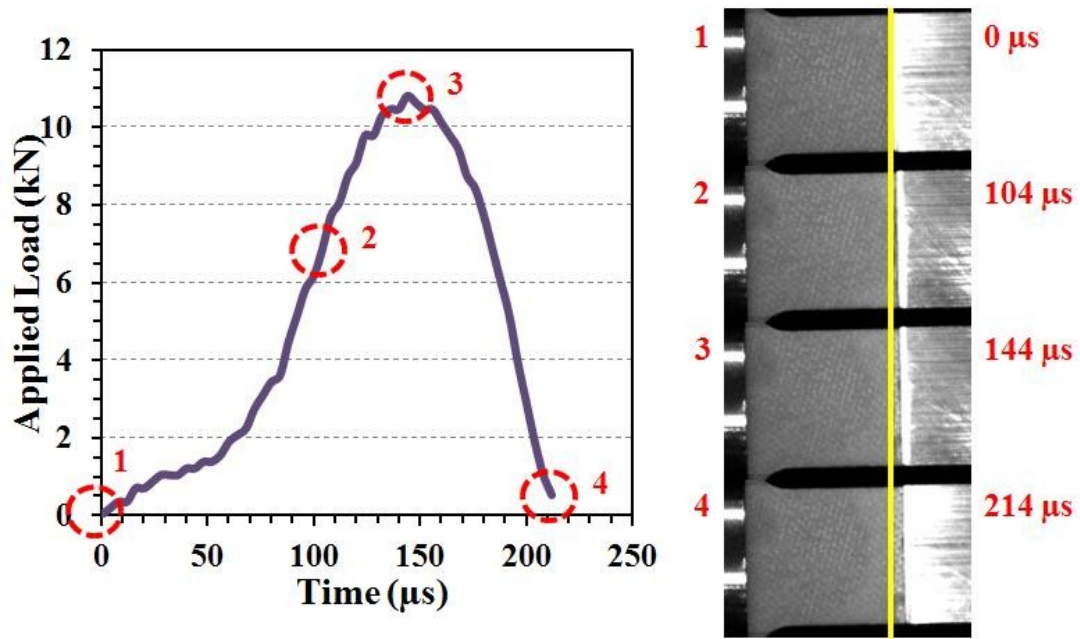


Figure 43: Load-time behavior of a bolted joint, $e/d=1$, subjected to impact with high speed images at 4 points along the loading event.

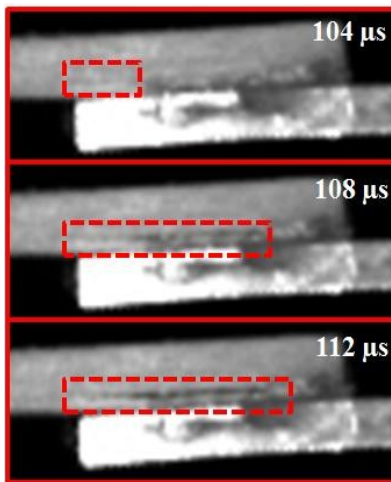


Figure 44: Interlaminar crack initiation in bonded joint from 104-112 μs.

difference in failure mode. While the statically loaded bonded joint failed in mixed mode failure, the impact loading resulted in an adherend failure. As the peak load is reached during interlaminar failure, a load path is still available through the adhesive. **Figure 44** shows the high speed images of a side profile of the bonded joint. An observable interlaminar crack develops at 104 μs and is prominent by 112 μs.

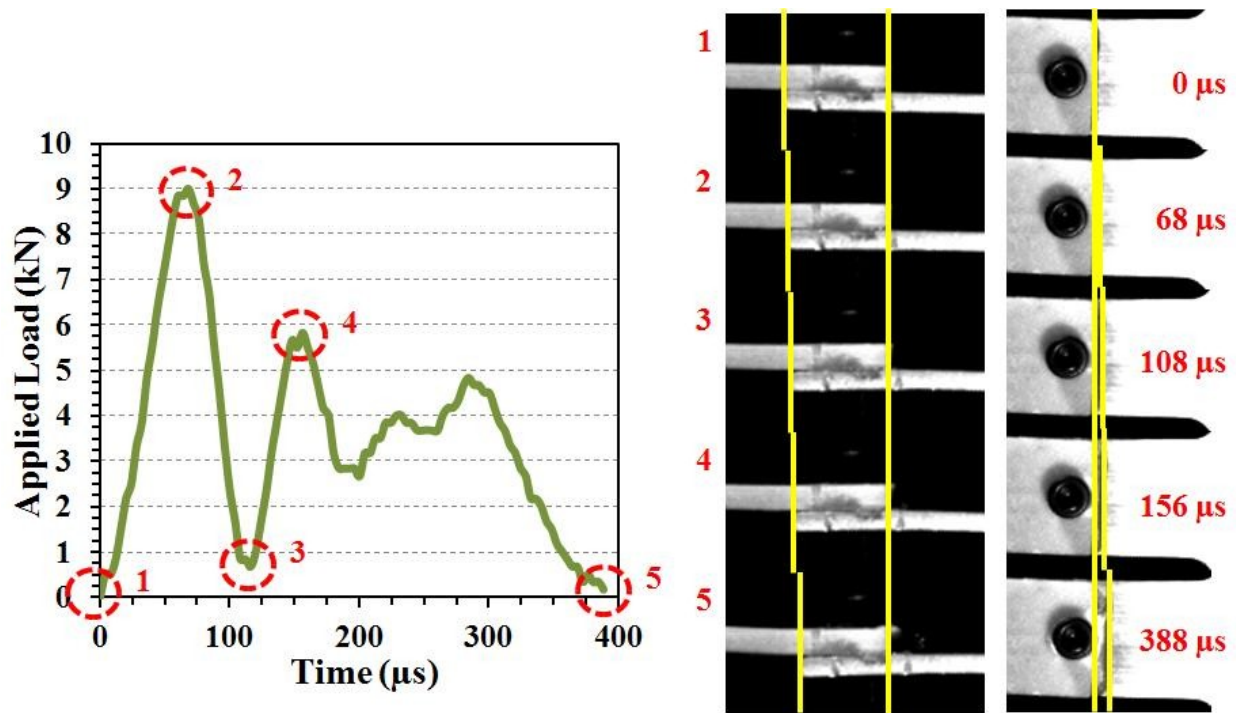


Figure 45: Load-time behavior of a hybrid joint, $e/d=1$, subjected to impact with high speed images at 5 points along the loading event.

Figure 45 shows the load-time behavior of a hybrid joint, $e/d = 1$, subjected to impact with high speed images at 5 points along the loading event. The initial loading occurs between points 1 and 2 and is linear in nature. In this region, the adhesive fails, there is partial slipping between the two materials, and composite damage initiates. Just like the impacted bolted joint, there is a coupling of phenomena that is generally separate and distinct under static loading. Full slip is achieved after $108 \mu\text{s}$ at point 3. The remaining region from points 3 to 5 demonstrate behavior similar to the impacted bolted joint. The second peak load at point 4 is on average 95% of the peak load attained by the purely bolted joint, accounting for the remainder of the composite strength that did not contribute to the initial loading. This shows that the initial loading phase is dominated by the adhesive both in profile and in peak load, and the rest of the behavior post-adhesive failure imitates that of the bolted joint, just as in the case of the static loading. Lastly, there are only minor differences in hybrid joint failure mode between static and

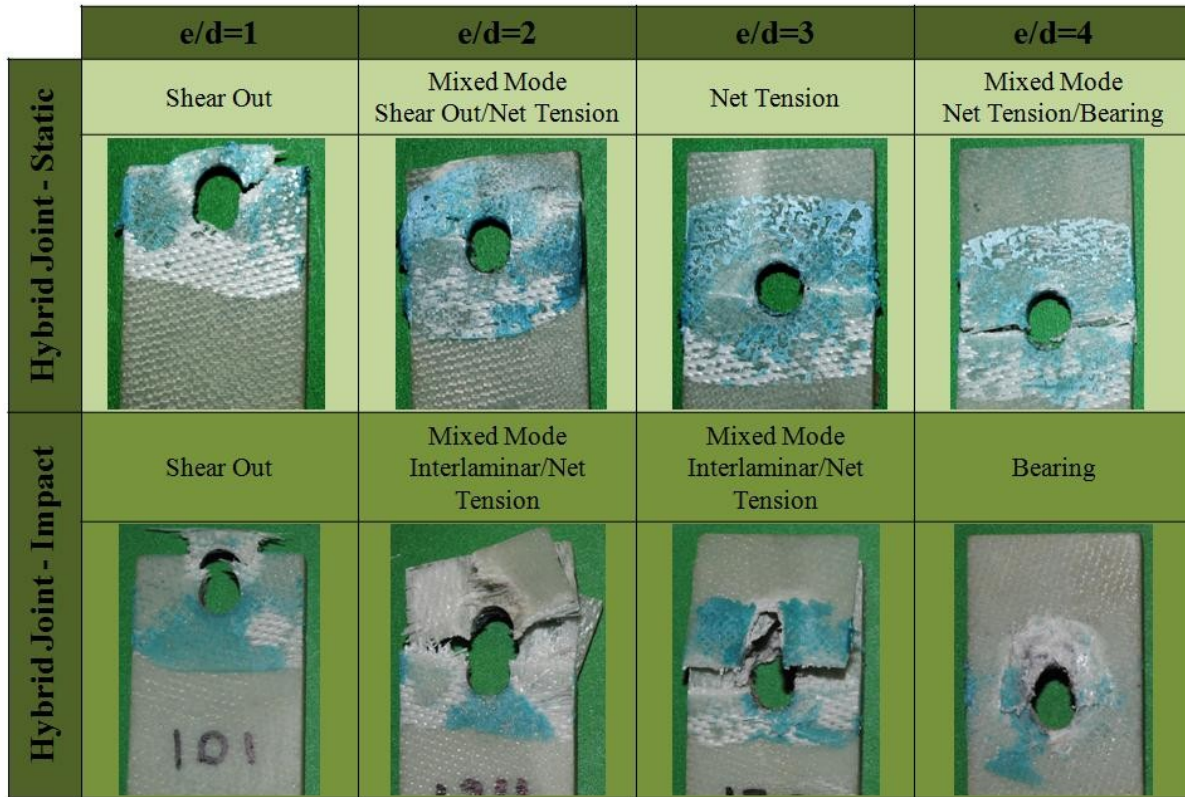


Figure 46 Observed failure modes for Aluminum/S2-glass hybrid joints, $e/d=1-4$, under static and impact loading.

impact testing as shown in **Figure 46**. Just as in the case with bolted joints, the major variations from static to impact loading is the presence of sub-surface deformation in the static condition and the presence of interlaminar shearing in the impact condition.

A comparison between bolted, bonded, and hybrid peak loads is shown in **Figure 47** and **Figure 48** for both static and impact loading conditions respectively. In the static case, peak load increases proportionally through $e/d=1-4$ for bolted joints while the hybrid peak load is constant at every e/d ratio and comparable to the bonded joint peak load. In the impact case, both bolted and hybrid joints experience greater peak load proportional to e/d and approach an asymptotic region between $e/d=3$ and 4. Hybrid joints in this region also exceed bonded joint peak load. In every joint type, peak load is higher in the impact loading condition than the static. In both cases, hybrid joints at $e/d=1$ demonstrate comparable strength to bolted joints at $e/d=4$.

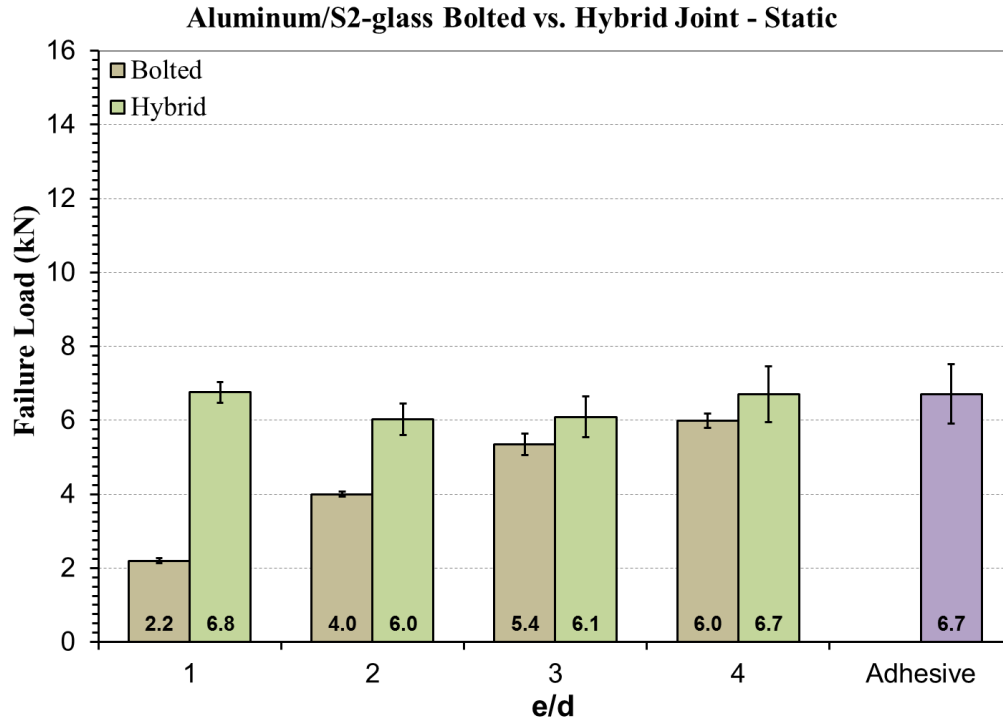


Figure 47: Peak loads of bolted, bonded, and hybrid joints, $e/d=1-4$, under static loading.

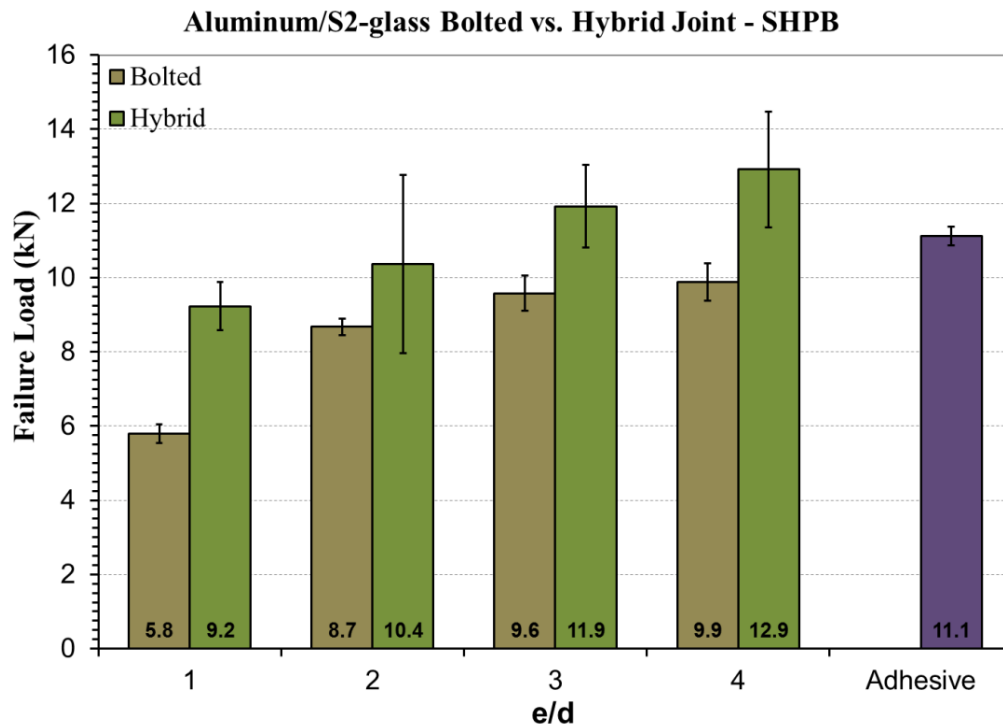


Figure 48: Failure loads of bolted, bonded, and hybrid joints, $e/d=1-4$, under static loading.

In addition to strength and failure mode, rate sensitivity is another performance metric useful in design. A joint that can perform the same irrespective of the loading condition induced is considered rate-insensitive and is preferable for design considerations. **Figure 49** shows the failure loads for bolted and hybrid joints with $e/d = 1-4$ at static, low velocity (intermediate), and impact loading. Intermediate failure load results performed by Venkadachalam (2014) are reproduced here with permission. It can be seen that the hybrid joint at $e/d = 1$ is the least rate sensitive than any of the other joint types or configurations, having the least difference in failure load from the static to the impact loading conditions at 28%. The bolted joint at $e/d = 1$ is on the opposite side of the spectrum, with a failure load variance of 62% across the loading rate range.

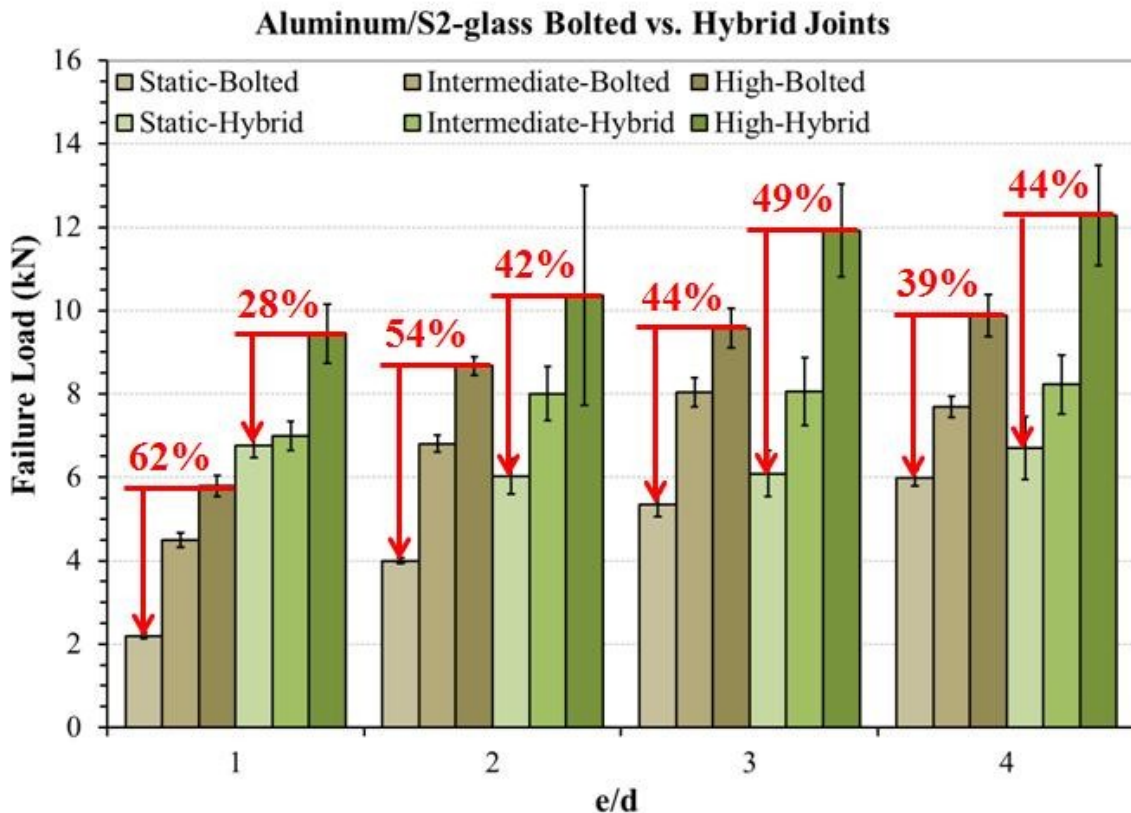


Figure 49: Failure loads of bolted and hybrid joints, $e/d = 1-4$, at static, low velocity (intermediate), and impact loading conditions.

3.4 Effect of Different Materials on Mechanical Behavior

Aluminum/E-glass (AL-E) single-lap bolted and hybrid joints tested in the SHTB for $e/d=1$ and 4 were compared against Aluminum/S2-glass (AL-S2) single-lap joints. **Figure 50** shows the resultant failure loads for each joint configuration. For both $e/d=1$ and 4, the bolted AL-E joint is weaker and the hybrid AL-E joint is stronger than their respective counterparts, signifying that the adhesive contributes more to the strength increase in the AL-E joint than it does for the AL-S2 one. This is a significant contribution given that E-glass composite fibers are considerably weaker than S2-glass composite fibers in tension. Another observation is that there is only a 1.5% strength increase from the hybrid AL-E joint at $e/d = 1$ to the one at $e/d = 4$, suggesting that the load to failure is dominated by the strength of the adhesive. Indeed the bonding affinity of the adhesive to the E-glass panel is greater than that towards the S2-glass



Figure 50: Failure loads of Aluminum/S2-glass and Aluminum/E-glass bolted and hybrid joints, $e/d=1$ and 4, under impact loading.

panel, as no adhesive-composite interfacial failure was observed in the AL-E hybrid joint. This may also indicate that surface preparation for the E-glass panel is not necessary, while that for the S2-glass panel, where adhesive-composite interfacial failure was observed, would have more of an effect on performance. More on surface preparation will be discussed in **Chapter 3.5**, “Effect of Surface Preparation on Mechanical Behavior.” Lastly, failure modes in the E-glass composite differed from those in the S2-glass composite as illustrated in **Figure 51**. In all joint configurations, the E-glass composite failed in net tension. Failure in this case is dependent largely in part to the strength of the composite in the axial direction which, for the 0°-90° fiber orientation in the E-glass, is attributed to the 0° fibers. It is expected that w/d would have to be larger in the E-glass composite than in the S2-glass composite in order to achieve maximum strength at any e/d ratio and for purely bearing damage to be possible.

	e/d=1 bolted	e/d=4 bolted	e/d=1 hybrid	e/d=4 hybrid
AL-S2 - Impact	Shear Out	Bearing	Shear Out	Bearing
				
AL-E - Impact	Mixed Mode Net Tension/Cleavage	Net Tension	Mixed Mode Net Tension/Cleavage	Mixed Mode Net Tension/Bearing
				

Figure 51: Observed failure modes for Aluminum/S2-glass and Aluminum/E-glass bolted and hybrid joints, $e/d = 1$ and 4, under impact loading.

The effect of alternative metal materials on mechanical behavior was investigated for Advanced High Strength Steel/S2-glass (AHSS-S2) single-lap bolted joints at $e/d = 1-4$ and hybrid joints at $e/d = 1$ and 2 and compared against similar AL-S2 joints. **Figure 52** shows the resultant failure loads for each joint configuration. It can be seen that AHSS-S2 bolted joints follow the same trend as the AL-S2 joints, where load to failure increases proportionally with e/d until it plateaus. The plateau point in the AHSS-S2 joint is to the left of that for the AL-S2 joint, having already attained maximum load capacity by $e/d = 3$ while the AL-S2 joint hasn't fully reached it with $e/d = 4$. Also, load to failure is higher at every e/d ratio for the AHSS-S2 joints. This can possibly be credited to a difference in rate sensitivity and energy absorption between the two metal materials. Unfortunately, the impact properties of both materials were not available at the tested loading rates and a more detailed explanation cannot be ascertained without those and a reliable model to understand the interaction of properties within the joint.

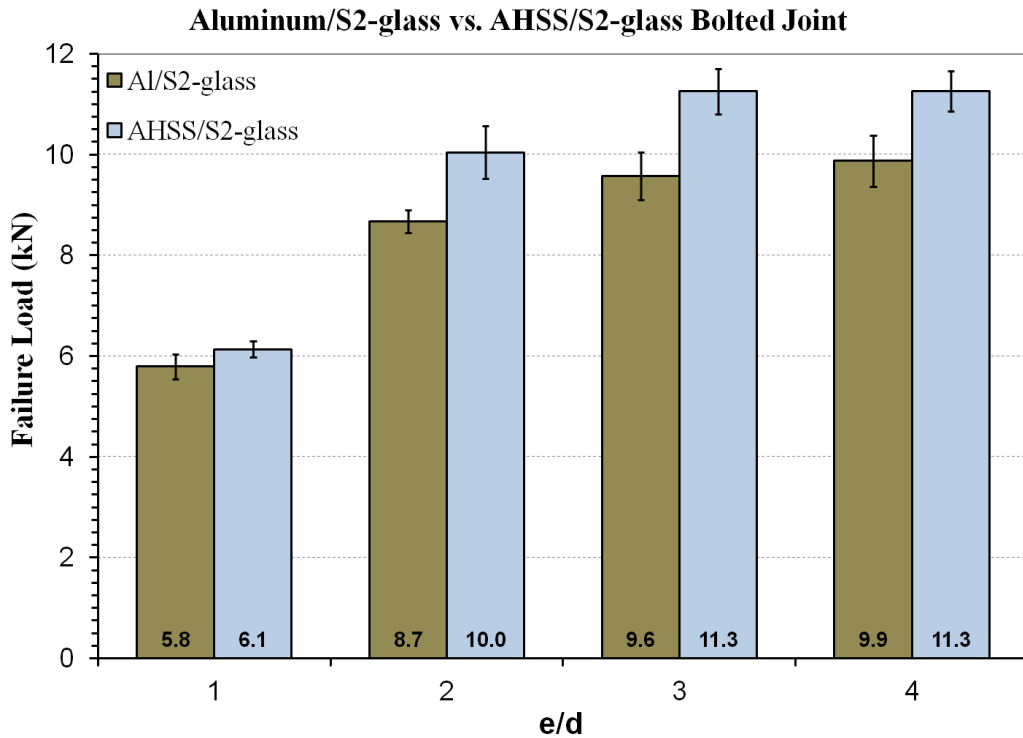


Figure 52: Failure loads of Aluminum/S2-glass and Advanced High Strength Steel/S2-glass bolted joints, $e/d = 1-4$, under impact loading.





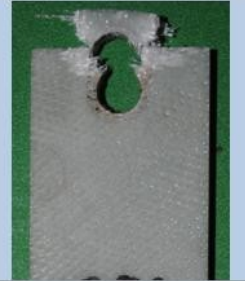

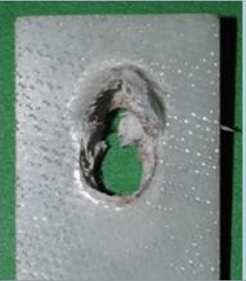

	$e/d=1$	$e/d=2$	$e/d=3$	$e/d=4$
AL-S2 - bolted	Shear Out	Mixed Mode Shear Out/Interlaminar Shear/Net Tension	Mixed Mode Bearing/Interlaminar Shear	Bearing
				
AHSS-S2 - bolted	Shear Out	Mixed Mode Shear Out/Bearing	Bearing	Bearing
				

Figure 53: Observed failure modes for Aluminum/S2-glass and Advanced High Strength Steel/S2-glass bolted joints, $e/d = 1-4$, under impact loading.

However, the failure modes shown in **Figure 53** do suggest that the difference in mechanical properties of the two metals do contribute to the difference in strength of the overall joint, since bearing failure is seen in the composite as early as $e/d = 2$ with the steel and not until $e/d = 3$ with the aluminum. This may be a result of a higher loading rate and possibly greater load transfer through the steel.

AHSS-S2 hybrid joints were also tested at $e/d = 1$ and 2. The failure loads of both joint configurations are shown in **Error! Reference source not found.** along with AHSS-S2 bolted joints for comparison. Unlike the AL-S2 joints, where a significant increase in load to failure is observed from bolted to hybrid, here the failure loads are identical. Observing the failure modes in **Figure 55**, it is clear from the complete adhesive failure at the adhesive-AHSS interface that

the adhesive did not contribute to the strength of the AHSS-S2 hybrid joint. This is a result of insufficient preparation of the steel surface. The effect of surface preparation on the strength of AHSS-S2 joints is outlined in the next subchapter, **Chapter 3.5**, “Effect of Surface Preparation on Mechanical Behavior.”

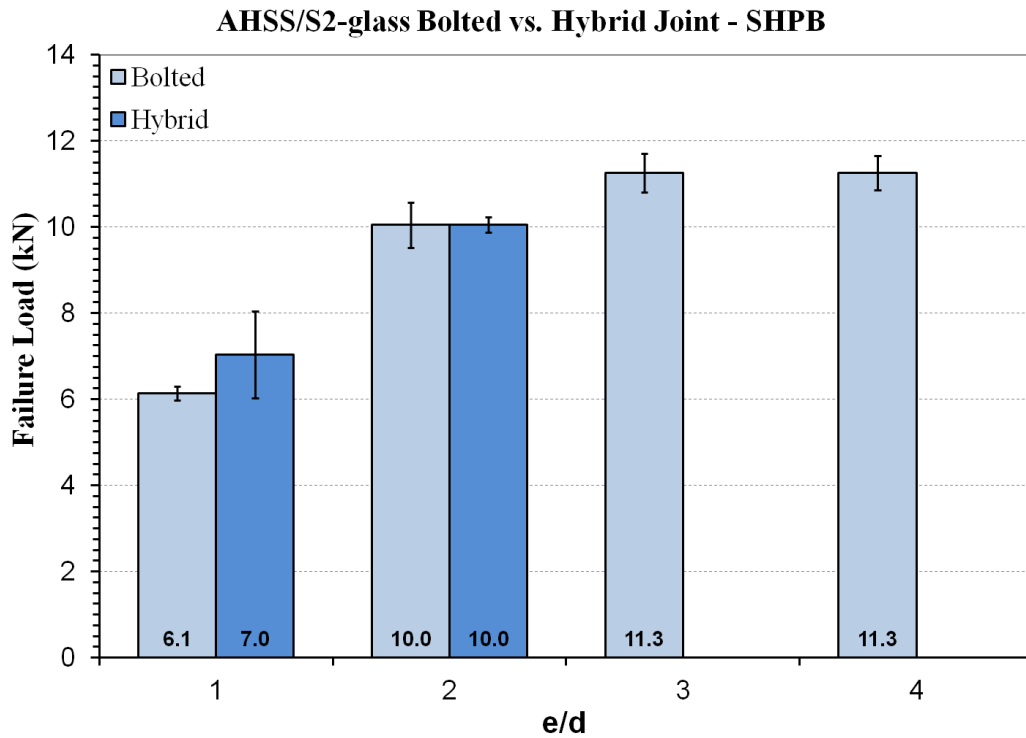


Figure 54: Failure loads of Advanced High Strength Steel/S2-glass bolted joints, $e/d = 1-4$, and hybrid joints, $e/d = 1$ and 2 , under impact loading.

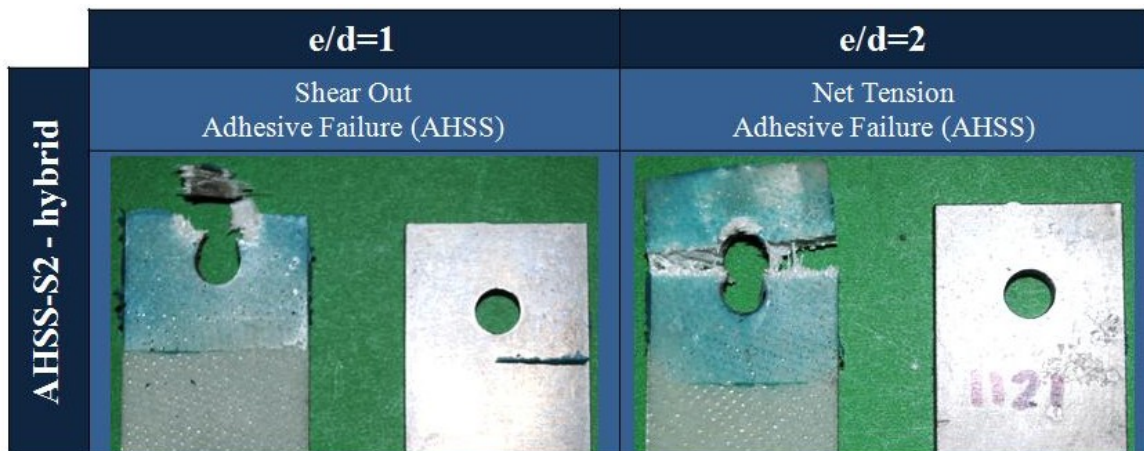


Figure 55: Observed failure modes for Advanced High Strength Steel/S2-glass hybrid joints, $e/d = 1$ and 2 , under impact loading.

3.5 Effect of Surface Preparation on Mechanical Behavior

All of the aforementioned tests involving FM-94 structural adhesive were performed on specimens with in-lab surface preparation methods. Aluminum 60601 surfaces were degreased, conditioned with an acid cleaner, sanded with silicon-carbide sandpaper, and neutralized prior to applying the adhesive. AHSS surfaces were prepared in the same manner, with an extra step to remove the mill scale via abrasive-grit blasting. A consequence of using commercial surface preparation is the cost involved. For this reason, experiments were carried out on both AL-S2 and AHSS-S2 hybrid joints with the adhesive manufacturer's surface preparation recommendations in order to determine whether or not the costly methods translate to better performance.

Aluminum 6061 surfaces were prepared in accordance with ASTM D2651-01, anodized with phosphoric acid in accordance with ASTM D3933-98, and primed with BR 127 Corrosion

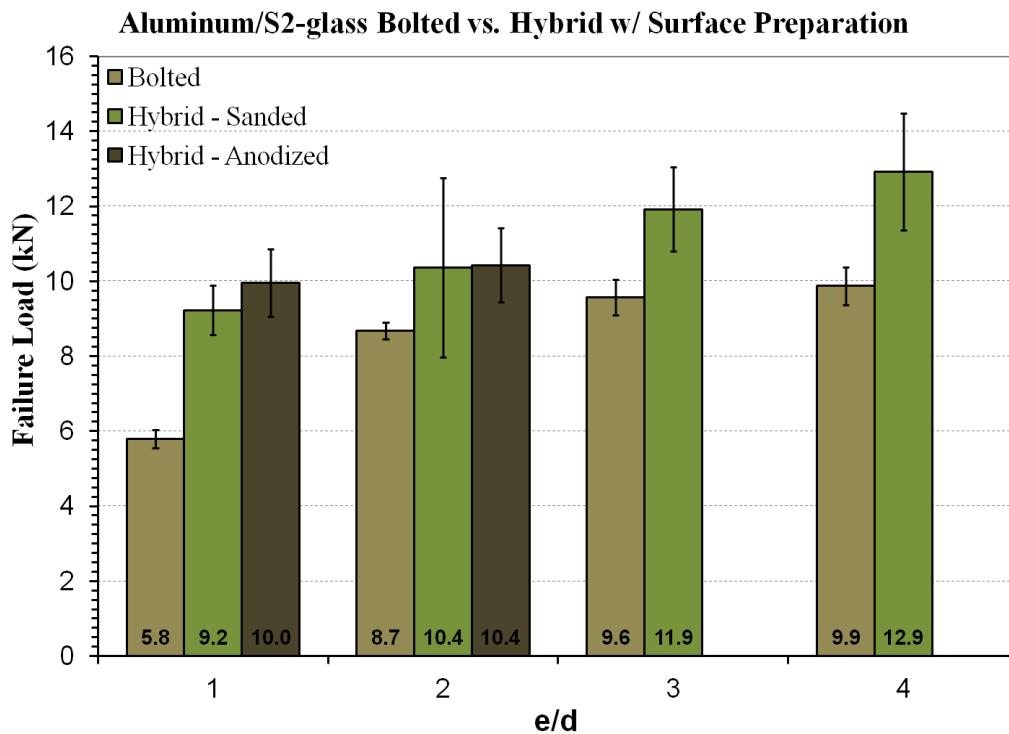


Figure 56: Failure loads of Aluminum/S2-glass bolted and hybrid joints, $e/d = 1-4$, and anodized hybrid joints, $e/d = 1$ and 2 , under impact loading.

Inhibiting Primer. **Figure 56** shows the failure loads of the AL-S2 bolted and hybrid joints, $e/d = 1-4$, and the anodized AL-S2 hybrid joints, $e/d = 1$ and 2. Anodizing proved to have only a marginal effect on the strength of the hybrid joints, with only an 8% increase in average failure load for $e/d = 1$, no increase for $e/d = 2$, and a 13% increase in confidence of the average failure load for $e/d = 2$. Although a more in depth cost-benefit analysis would have to be performed, the minor increase in performance suggests that commercial surface preparation methods are not cost effective for aluminum

AHSS surfaces were also prepared in accordance with ASTM D2651-01 and primed with BR 127 Corrosion Inhibiting Primer for AHSS-S2 hybrid joints, $e/d = 1$ and 2. **Figure 57** illustrates the failure load results compared against bolted, $e/d = 1-4$, and hybrid joints with in-lab sandblasting preparation, $e/d = 1$ and 2. A significant increase in failure load was observed

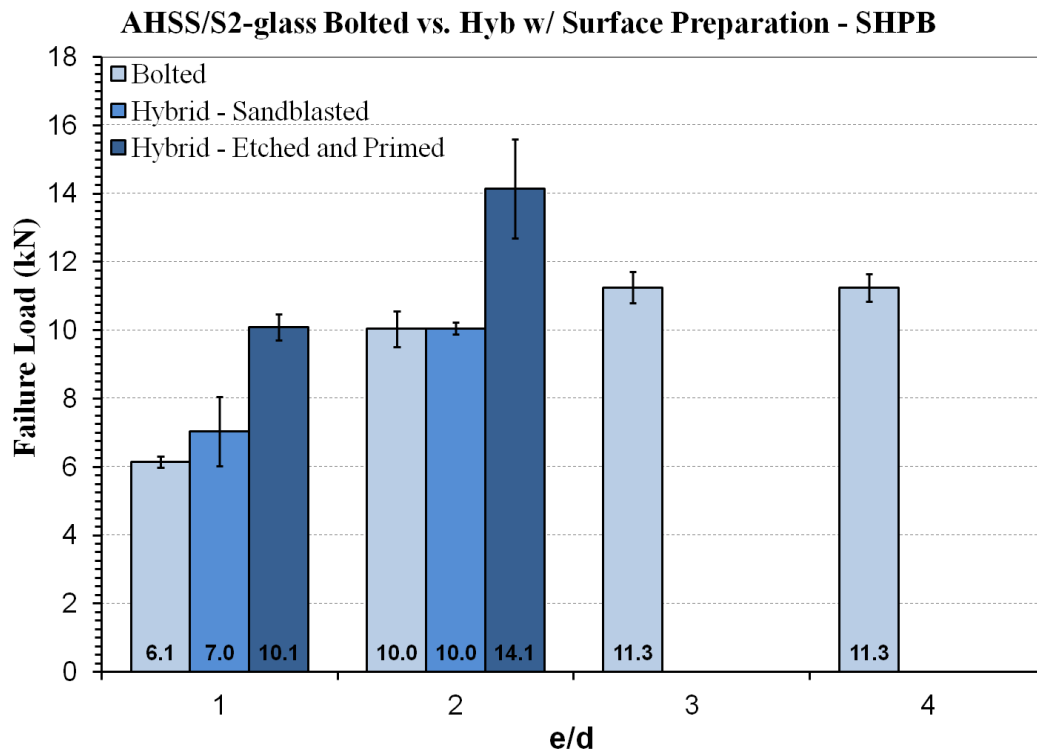


Figure 57: Failure loads of Advanced High Strength Steel/S2-glass bolted joints, $e/d = 1-4$, and hybrid joints with and without commercial surface preparation, $e/d = 1$ and 2, under impact loading.

for both $e/d = 1$ and 2 at 43% and 41% respectively. In both cases, failure was mostly observed in the S2-glass material with no cohesive or adhesive failures. While commercial surface preparation had little to no effect on the strength of AL-S2 hybrid joints, it proves to be beneficial if not necessary for AHSS-S2 hybrid joints.

3.6 Effect of Elevated Temperature on Mechanical Behavior

While great efforts were taken to develop a novel technique for performing elevated temperature experiments in a SHTB (described in **Chapters 2.2** and **2.3**), only a few results were captured as a result of schedule constraints on the project. **Figure 58** shows the failure loads of AL-S2 hybrid joints at room temperature and 80°C for $e/d = 1$ and 4 (with exception of hybrid $e/d = 4$ due to schedule). All joint configurations experienced a significant 20-30% decrease in

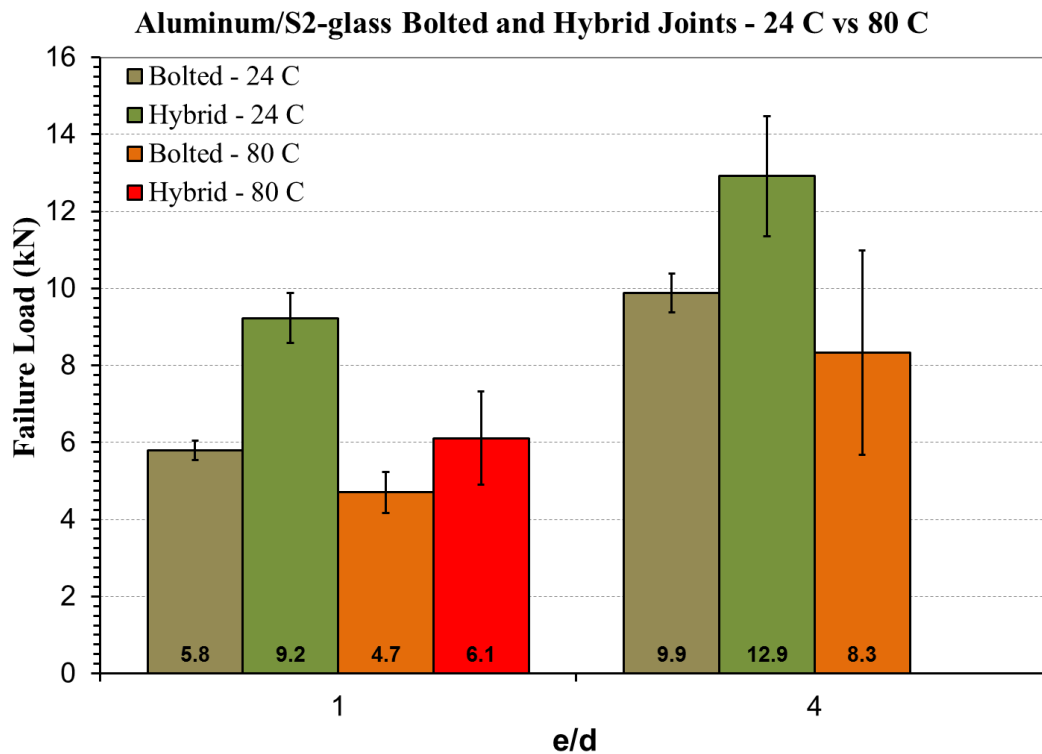


Figure 58: Failure loads of Aluminum/S2-glass bolted and hybrid joints, $e/d = 1$ and 4 , at room temperature and 80°C under impact loading.

failure load at 80°C. Since glass transition temperature for S2-glass fibers is 846°C, the reduction in strength is most likely not due to any effect of temperature on the fibers. However, when considering the glass transition temperature of the SC-15 resin at 95°C, it is likely that the resin was in the softening region at 80°C and therefore susceptible to reduced strength. Lastly, the FM-94 adhesive manufacturer lists the shear strength as 46.6 MPa at 24°C and 34.8 MPa at 82°C, approximately a 25% reduction in strength that would have impacted the overall strength of the joint. Since elevated temperatures affect both bolted and hybrid joints alike, using a particular resin or adhesive would depend on application of the joint structure.

CHAPTER 4: Conclusion

4.1 Concluding Remarks

A careful analysis has been performed on metal-composite single-lap joints with investigations into the effects of joining method, geometry, loading rate, material type, surface preparation, and elevated temperature on mechanical behavior. A case has been presented here that when hybrid joints are permissible in a structure, such as in the case where easy disassembly and reassembly is not required and environmental effects are limited with respect to the type of adhesive used, that they are superior to both bolted and bonded joints. Reducing the bolt hole edge distance by a factor of 4 in hybrid joints to achieve the same strength as the bolted joint directly translates to increased cost savings in required material quantities. Of course, the cost of surface preparation for adhesive bonding must be considered to truly assess the cost benefit of hybrid joints. This depends on the type of materials used, since the current study asserts that expensive commercial surface preparation is required for advanced high strength steel applications while it is not necessary for aluminum applications (when using FM-94 structural adhesive only). Lastly, material combinations must be selected carefully when considering applications in elevated temperatures, since composite resins and adhesives can be significantly affected by them.

With so many material and geometric factors affecting a simple single-lap joint, it is difficult to outline general design guidelines that apply beyond the specific joint types studied in this investigation. However, this work has helped to establish a precedent for testing large scale structural components at high loading rates as well as elevated temperatures. Additionally, the careful comparison between static and impact loading has further bridged the knowledge gap involving differences in mechanical response and has further emphasized the need to pursue

dynamic studies in the future. Lastly, the study serves as a solid foundation for developing and validating analytical and numerical models that will be more useful to design.

4.2 Future Scope of Work

This work is a launching platform for numerous other studies. Countless parametric studies of other key parameters of joints under impact loading need to be investigated including bolt preload, ply orientation in composites, bolt hole clearance, and other joining methods (ex: double lap and T-joint). These can be further extrapolated to different loading conditions including compression, torsion, multi-axial, and fatigue. Ultimately the physics governing the mechanical behavior of structural joints needs to be understood in order to develop more sophisticated models that have predictive qualities. Since it is impossible to experimentally test every possible joint configuration, the future of joint design lies in numerical models that accurately predict response and performance.

REFERENCES

REFERENCES

- [1] Matthews, F. L., Kilty, P. F., and Godwin, E. W., 1982, "A review of the strength of joints in fibre-reinforced plastics. Part 2. Adhesively bonded joints," *Composites*, **13**(1), pp. 29–37.
- [2] Hart-Smith, L. J., 1982, *Design Methodology for Bonded-Bolted Composite Joints. Volume I. Analysis Derivations and Illustrative Solutions*.
- [3] Hart-Smith, L. J., 1985, "Bonded-bolted composite joints," *J. Aircr.*, **22**(11), pp. 993–1000.
- [4] Kretsis, G., and Matthews, F. L., 1985, "The strength of bolted joints in glass fibre/epoxy laminates," *Composites*, **16**(2), pp. 92–102.
- [5] Xiao, Y., and Ishikawa, T., 2005, "Bearing strength and failure behavior of bolted composite joints (part I: Experimental investigation)," *Compos. Sci. Technol.*, **65**(7–8), pp. 1022–1031.
- [6] Collings, T. A., 1977, "The strength of bolted joints in multi-directional cfrp laminates," *Composites*, **8**(1), pp. 43–55.
- [7] Smith, P. A., Pascoe, K. J., Polak, C., and Stroud, D. O., 1986, "The behaviour of single-lap bolted joints in CFRP laminates," *Compos. Struct.*, **6**(1–3), pp. 41–55.
- [8] Arnold, W. S., Marshall, I. H., and Wood, J., 1990, "Optimum design considerations for mechanically fastened composite joints," *Compos. Struct.*, **16**(1–3), pp. 85–101.
- [9] Chamis, C. C., 1990, "Simplified Procedures for Designing Composite Bolted Joints," *J. Reinf. Plast. Compos.*, **9**(6), pp. 614–626.
- [10] Cooper, C., and Turvey, G. J., 1995, "Effects of joint geometry and bolt torque on the structural performance of single bolt tension joints in pultruded GRP sheet material," *Compos. Struct.*, **32**(1–4), pp. 217–226.
- [11] Okutan, B., Aslan, Z., and Karakuzu, R., 2001, "A study of the effects of various geometric parameters on the failure strength of pin-loaded woven-glass-fiber reinforced epoxy laminate," *Compos. Sci. Technol.*, **61**(10), pp. 1491–1497.
- [12] Okutan, B., 2002, "The effects of geometric parameters on the failure strength for pin-loaded multi-directional fiber-glass reinforced epoxy laminate," *Compos. Part B Eng.*, **33**(8), pp. 567–578.
- [13] Kelly, G., and Hallström, S., 2004, "Bearing strength of carbon fibre/epoxy laminates: effects of bolt-hole clearance," *Compos. Part B Eng.*, **35**(4), pp. 331–343.
- [14] Pakdil, M., Sen, F., Sayman, O., and Benli, S., 2007, "The Effect of Preload on Failure Response of Glass-Epoxy Laminated Composite Bolted-Joints with Clearance," *J. Reinf. Plast. Compos.*

- [15] Sayman, O., Siyahkoc, R., Sen, F., and Ozcan, R., 2007, "Experimental Determination of Bearing Strength in Fiber Reinforced Laminated Composite Bolted Joints under Preload," *J. Reinf. Plast. Compos.*, **26**(10), pp. 1051–1063.
- [16] Thoppul, S. D., Finegan, J., and Gibson, R. F., 2009, "Mechanics of mechanically fastened joints in polymer–matrix composite structures – A review," *Compos. Sci. Technol.*, **69**(3–4), pp. 301–329.
- [17] Sen, O., 2011, "Analysis of the study of material behavior at impact rates of strain," M.S., Michigan State University.
- [18] Ramesh, K. T., 2008, "High Rates and Impact Experiments," *Springer Handbook of Experimental Solid Mechanics*, W.N.S.J. Prof, ed., Springer US, pp. 929–960.
- [19] Al-Mousawi, M. M., Reid, S. R., and Deans, W. F., 1997, "The use of the split Hopkinson pressure bar techniques in high strain rate materials testing," *Proc. Inst. Mech. Eng. Part C J. Mech. Eng. Sci.*, **211**(4), pp. 273–292.
- [20] Hopkinson, B., 1914, "A Method of Measuring the Pressure Produced in the Detonation of High Explosives or by the Impact of Bullets," *Proc. R. Soc. Lond. Ser. A*, **89**(612), pp. 411–413.
- [21] Gama, B. A., Lopatnikov, S. L., and Gillespie, J., John W, 2004, "Hopkinson bar experimental technique: A critical review," *Appl. Mech. Rev.*, **57**(4), pp. 223–250.
- [22] Davies, R. M., 1948, "A Critical Study of the Hopkinson Pressure Bar," *Philos. Trans. R. Soc. Lond. Ser. Math. Phys. Sci.*, **240**(821), pp. 375–457.
- [23] Kolsky, H., 1949, "An Investigation of the Mechanical Properties of Materials at very High Rates of Loading," *Proc. Phys. Soc. Sect. B*, **62**(11), p. 676.
- [24] Harding, J., Wood, E. O., and Campbell, J. D., 1960, "Tensile Testing of Materials at Impact Rates of Strain," *J. Mech. Eng. Sci.*, **2**(2), pp. 88–96.
- [25] Ogawa, K., 1984, "Impact-tension compression test by using a split-Hopkinson bar," *Exp. Mech.*, **24**(2), pp. 81–86.
- [26] Benassi, F., and Alves, M., 2006, "Pulse shaping in the split Hopkinson pressure bar test," *Proc IV Natl. Congr. Mech. Eng.*
- [27] Frew, D. J., Forrestal, M. J., and Chen, W., 2005, "Pulse shaping techniques for testing elastic-plastic materials with a split Hopkinson pressure bar," *Exp. Mech.*, **45**(2), pp. 186–195.
- [28] Vecchio, K. S., and Jiang, F., 2007, "Improved Pulse Shaping to Achieve Constant Strain Rate and Stress Equilibrium in Split-Hopkinson Pressure Bar Testing," *Metall. Mater. Trans. A*, **38**(11), pp. 2655–2665.
- [29] Chen, W. W., and Song, B., 2010, *Split Hopkinson (Kolsky) Bar: Design, Testing and Applications*, Springer Science & Business Media.

[30] 2006, “MTS 810 & 858 Material Testing Systems.”

[31] Kweon, J.-H., Jung, J.-W., Kim, T.-H., Choi, J.-H., and Kim, D.-H., 2006, “Failure of carbon composite-to-aluminum joints with combined mechanical fastening and adhesive bonding,” *Compos. Struct.*, **75**(1–4), pp. 192–198.